Voltage imaging identifies spinal circuits that modulate locomotor adaptation in zebrafish

Highlights

- Voltage imaging reveals the dynamics of zebrafish spinal motor circuits

- A ventral glutamatergic neuron population modulates swim strength

- Tail beat strength and bout duration are controlled separately from beat frequency

Authors

Urs L. Böhm, Yukiko Kimura, Takashi Kawashima, Misha B. Ahrens, Shin-ichi Higashijima, Florian Engert, Adam E. Cohen

Correspondence

cohen@chemistry.harvard.edu

In brief

Böhm and co-workers apply light-sheet voltage imaging to the spinal cords of zebrafish swimming in a virtual environment and identify a subpopulation of glutamatergic neurons that modulates swim strength and bout duration without affecting tail beat frequency.

CellPress

Neuron

CellPress

Article

Voltage imaging identifies spinal circuits that modulate locomotor adaptation in zebrafish

Urs L. Böhm,[1] Yukiko Kimura,[2] Takashi Kawashima,[3,6] Misha B. Ahrens,[3] Shin-ichi Higashijima,[2] Florian Engert,[4] and Adam E. Cohen[1,5,7,*]

[1]Department of Chemistry and Chemical Biology, Harvard University, Cambridge, MA 02138, USA
[2]National Institutes of Natural Sciences, Okazaki Institute for Integrative Bioscience, National Institute for Physiological Sciences, Okazaki, Aichi 444-8787, Japan
[3]Janelia Research Campus, Howard Hughes Medical Institute, Ashburn, VA 20147, USA
[4]Department of Molecular and Cellular Biology, Harvard University, Cambridge, MA 02138, USA
[5]Department of Physics, Harvard University, Cambridge, MA 02138, USA
[6]Present address: Department of Neurobiology, Weizmann Institute of Science, Rehovot, Israel
[7]Lead contact
*Correspondence: cohen@chemistry.harvard.edu
https://doi.org/10.1016/j.neuron.2022.01.001

SUMMARY

Motor systems must continuously adapt their output to maintain a desired trajectory. While the spinal circuits underlying rhythmic locomotion are well described, little is known about how the network modulates its output strength. A major challenge has been the difficulty of recording from spinal neurons during behavior. Here, we use voltage imaging to map the membrane potential of large populations of glutamatergic neurons throughout the spinal cord of the larval zebrafish during fictive swimming in a virtual environment. We characterized a previously undescribed subpopulation of tonic-spiking ventral V3 neurons whose spike rate correlated with swimming strength and bout length. Optogenetic activation of V3 neurons led to stronger swimming and longer bouts but did not affect tail beat frequency. Genetic ablation of V3 neurons led to reduced locomotor adaptation. The power of voltage imaging allowed us to identify V3 neurons as a critical driver of locomotor adaptation in zebrafish.

INTRODUCTION

Dynamically adapting motor output is an essential function of vertebrate locomotor control. Animals must adjust the force of their muscles to change speed or to respond to changes in internal or external forces. The core networks that generate the rhythmic activity essential for locomotion have been extensively studied in many model systems (Grillner and Manira, 2015). Much less is understood about how these networks are dynamically modulated. One technical challenge is the difficulty of spinal cord recordings during behavior. Rodent spinal cords are hard to access optically or electrically *in vivo*, and organisms more amenable to optical methods such as *Xenopus* tadpoles or zebrafish larvae have dynamics faster than the temporal resolution of Ca^{2+} imaging. Thus, population-wide measurements of membrane potential in locomotor circuits have so far only been possible in invertebrate preparations using voltage-sensitive dyes (Bruno et al., 2015; Tomina and Wagenaar, 2017).

Voltage imaging using genetically encoded voltage indicators (GEVIs) has the potential to overcome these limitations. Recent advances in sensors (Abdelfattah et al., 2019; Adam et al., 2019; Chien et al., 2021; Gong et al., 2015; Piatkevich et al., 2019; Villette et al., 2019), optics (Fan et al., 2020), and analytical tools (Cai et al., 2021; Xie et al., 2021) have made it possible to

record subthreshold and spiking activity from multiple cells *in vivo*. These advances open the possibility to map voltage dynamics across a population and to characterize their activity in an unbiased way.

At 5 days post fertilization (dpf), zebrafish larvae show a range of behaviors, including fast and slow forward swimming, turns, escape responses, and prey capture (Budick and O'Malley, 2000; Marques et al., 2018). Slow forward swimming occurs in a "beat-and-glide" mode comprising brief swim bouts (200–400 ms, tail beat frequency 20–70 Hz), separated by interbout glide intervals of variable length (400 ms to several seconds) (Buss and Drapeau, 2001). A change in mean velocity can arise through a change in tail beat frequency, a change in cycle amplitude or force, or a change in the duty cycle of swim bouts relative to glide intervals (Ahrens et al., 2012; Kawashima et al., 2016; Portugues and Engert, 2011; Severi et al., 2014). It has been shown that distinct populations of premotor excitatory interneurons are recruited at different tail beat frequencies (Ljunggren et al., 2014; McLean et al., 2007, 2008; Wahlstrom-Helgren et al., 2019), but the spinal mechanisms underlying adaptation in swim force and bout duration are currently unknown.

Here we use light-sheet voltage imaging to map neural activity in the zebrafish spinal cord during slow forward swimming in a virtual environment. We characterized in detail the patterns of

network activity and subcellular action potential propagation across all glutamatergic subtypes. In a previously uncharacterized cell type—spinal V3 interneurons—we found that activity was correlated with swimming but in a nonrhythmic way. V3 neurons are defined by sim1 expression, and in mice, V3 neurons make connections to motor neurons both ipsi- and contralaterally (Chopek et al., 2018; Zhang et al., 2008). Loss-of-function and optogenetic experiments in mice suggested a role of V3 neurons in left-right coordination and robustness of locomotory activity (Danner et al., 2019; Zhang et al., 2008).

We found that V3 neuron activity during swimming correlated with the strength and duration of each swim bout. We used optogenetic activation and genetically targeted ablations of V3 neurons to characterize the functional role of V3 neurons in larval zebrafish and showed that V3 neurons act as a modulator of swimming, primarily by affecting swim strength and bout length. These findings revealed a new mechanism by which spinal networks modify locomotion and demonstrate the power of voltage imaging to uncover previously inaccessible neural dynamics.

RESULTS

Distinct oscillatory and nonoscillatory subpopulations of excitatory spinal neurons

To evoke patterns of neural activity associated with naturalistic swimming in immobile fish, we implemented virtual reality (VR) feedback (Ahrens et al., 2013; Vladimirov et al., 2014) in a custom-built light-sheet microscope (Figures 1A and S1). Fish were paralyzed with 1 mg/mL α-bungarotoxin and placed in the recording chamber. Electrical recordings from a ventral nerve root (VNR) on one side of the fish were processed in real time to calculate a fictive swim strength, which depended on the VNR amplitude and frequency (STAR Methods). To evoke robust swim responses, we created a VR environment, and we emulated a condition where the animal was swept backward by a constant water current. Specifically, the swim strength was scaled by a user-selected feedback gain to obtain a fictive swim speed and then subtracted from the motion of a drifting grating projected from below. This setup provided independent control of the baseline grating drift speed and the feedback gain and helped to invoke consistent fictive swim bouts interspersed with rests. Fictive swimming produced average cycle frequencies per bout of 23 ± 4 Hz (mean ± SD, n = 840 bouts, 9 fish), an average bout duration of 0.4 ± 0.4 s and average interbout intervals of 0.8 ± 0.8 s.

To visualize neural dynamics in fish performing fictive swimming, we generated the transgenic line *Tg(UAS:zArchon1-GFP)* to express the voltage sensor zArchon1 (Piatkevich et al., 2018). We then used the *Tg(vGlut2a:Gal4)* driver line (Satou et al., 2013) to drive expression of zArchon1 in glutamatergic spinal neurons of 5–6 dpf zebrafish. Sensor expression in the transgenic line showed excellent membrane localization and closely resembled previous reports with transient expression (Piatkevich et al., 2018) (Figure 1B). We used wide-field light-sheet imaging to record the membrane voltage of the glutamatergic neurons at a 1-kHz frame rate, while larvae performed fictive forward swims. We routinely recorded from >10 neurons in parallel (11 ± 7 active cells per field of view, mean ± SD, max: 29, n = 339 cells, 9 fish) (Figure 1C).

The voltage waveforms broadly fell into two classes: in some neurons, membrane potential oscillated at constant phase relative to the VNR signal during swim bouts (Video S1); in others, membrane potential showed clear spiking but did not oscillate (Figure 1C; Video S2). To categorize the neurons and quantify the amplitude and phase of the subthreshold oscillations, we used the VNR signal as a time base and calculated the VNR-triggered average membrane voltage during a swim cycle (Figure 1D). Neurons with oscillatory subthreshold voltages were clustered in the middle of the spinal cord along the dorsoventral axis, above the central canal (Figure 1E). The phases of the oscillating neurons fell into two groups 180° phase shifted relative to each other and localized to the left and right halves of the spinal cord, respectively (Figures 1F and 1G).

Simultaneous voltage imaging of multiple neurons along a 480-μm-long segment of the spinal cord revealed a position-dependent phase delay with a mean slope of 0.51π radians/mm (or 0.087 m/s at an average cycle frequency of 22.6 Hz), corresponding to a wavelength of 3.9 mm (Figure 1H). At 5–6 dpf, we measured a muscle segment size of 93 ± 8 μm (mean ± SD), implying a phase delay of 2.4% ± 0.2% per segment. Previously published VNR recordings reported a similar phase delay of motor output (2.6% ± 1.7% per segment) (Masino and Fetcho, 2005). The location and dynamics of the oscillatory neurons indicate that these neurons are primarily V0v (MCoD) and V2a (CiD) premotor excitatory interneurons, which have been reported to show oscillatory dynamics similar to our observations (McLean et al., 2008). These neurons have a spike width of approximately 1 ms (McLean et al., 2008), below the Nyquist frequency of our recordings. Consequently, spikes were only detectable in the most strongly expressing cells (Figure S2).

The second population consisted of distinctively nonoscillating neurons. This population comprised a subpopulation clustered at the very ventral margin of the spinal cord and a more scattered subpopulation at the dorsal margin (Figures 1E and S3). We subdivided the nonoscillating neurons based on whether their spike rate was higher during swim bouts or between swim bouts (STAR Methods; Figure S3). Most of the ventral population spiked more during swim bouts while the dorsal population contained relatively more neurons that spiked more during interbout intervals (Figure 1E). Because of their clear anatomical localization and distinctive firing patterns, we focused further studies on the ventral subpopulation.

The location in the spinal cord and glutamatergic phenotype of the ventral bout-active neurons, suggested them to be V3 (VeMe) neurons. V3 neurons have been morphologically described as ventral glutamatergic neurons with a descending axon and molecularly defined by the expression of the transcription factor *sim1a* (Hale et al., 2001; Higashijima et al., 2004). These cells are suggested to be homologs of mammalian V3 interneurons (Goulding, 2009). We crossed a vGlut2a:GFP line with *Tg(sim1a:loxP-DsRed-loxP-DTA)* to label glutamatergic neurons green and V3 neurons red (without any Cre expression, which would activate the diphtheria toxin A and ablate expressing cells). Of the glutamatergic neurons below the central canal, 76% (133 of 174 neurons, N = 3 fish, Figure S4) were also DsRed positive. This result implies that at least 76% of ventral glutamatergic neurons were V3, in line with previous reports (Wiggin et al., 2021; Yang et al., 2010). The
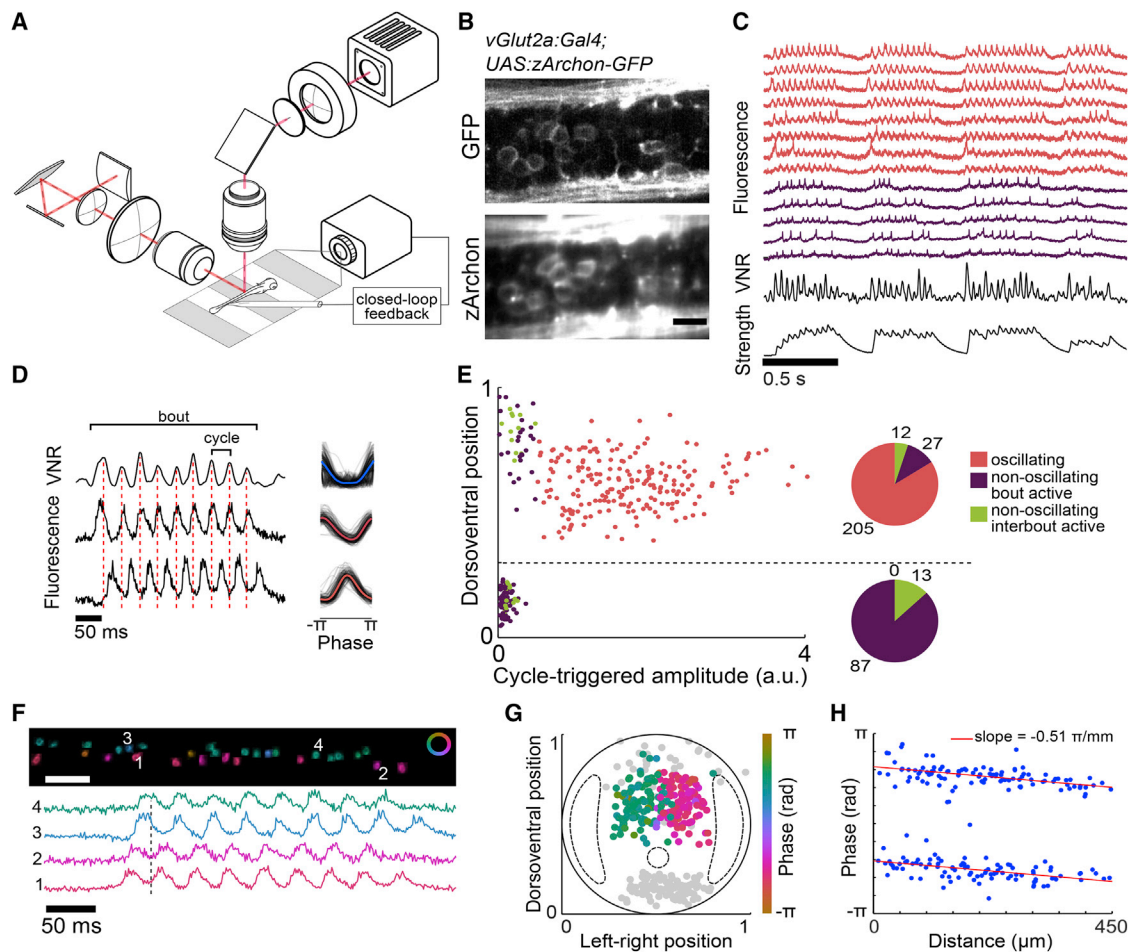
Neuron
Article

CellPress

Figure 1. Voltage imaging in spinal neurons during fictive swimming

(A) Schematic of the light-sheet microscope, ventral nerve root recording, and closed-loop visual feedback.

(B) zArchon1-GFP expression in the *Tg(vGlut2a:Gal4; UAS:zArchon1-GFP)* transgenic line. Top: two-photon image of GFP expression marker; bottom: light-sheet image of zArchon1 fluorescence in the same focal plane. Scale bar, 10 μm.

(C) Fluorescence traces showing simultaneously recorded neurons (n = 13) divided into oscillating (red) and nonoscillating (purple) activity patterns. Bottom: processed VNR signal and derived swim strength.

(D) Left: VNR signal and fluorescence of two simultaneously recorded oscillating cells. Right: VNR-cycle-triggered averages.

(E) Relationship between cycle-triggered amplitude and dorsoventral position for n = 344 neurons, 9 fish. The pie charts show the distribution of activity types in the dorsal and ventral subpopulations.

(F) Phase map of simultaneously recorded oscillating neurons. Cell bodies are colored according to their phase relative to the VNR signal. Scale bar, 50 μm.

(G) Transverse view showing cell-body positions of oscillating neurons, color coded by phase relative to VNR. Nonoscillating cells in gray; dotted lines indicate position of the lateral neuropil region and the central canal.

(H) Relationship of average phase and cell-body position along the rostro-caudal axis. The two populations indicate cell bodies on the left and the right side of the spinal cord. The slope indicates the phase delay along the tail. Slope = −0.51 ± 0.06 π radians/mm (mean ± SEM), r^2 = 0.96. See also Figures S1–S3.

remaining 24% of the neurons might reflect a minor non-V3 ventral glutamatergic subpopulation, or they could reflect partial silencing of the *sim1a* marker in some cells at the time of measurement. Because we did not observe distinct subclasses of ventral neurons based on the firing patterns, we hereafter refer to the ventral glutamatergic neurons as V3.

V3 neuron spiking, subthreshold activity, and morphology

We used our extensive dataset of membrane voltage recordings to further characterize the behavior of the V3 neurons. At the start of a

swim bout, V3 neurons rapidly depolarized, and the spike rate ramped up during the first swim cycle (time constant for spiking onset: τ_{on} = 65 ± 4 ms) (Figure 2A). At the end of a swim bout, the VNR signal ended abruptly, but the mean V3 firing rate gradually decreased, starting before the end of the swim bout, without any apparent discontinuity at the end of swimming (τ_{off} = 137 ± 18 ms). The subthreshold voltages also showed fast depolarization at the start of a swim bout and gradual repolarization at the end (Figure 2A). In contrast to the oscillating dorsal population, neither the subthreshold voltage (Figure 1E) nor the spike rate (Figure 2B) oscillated in synchrony with the VNR during swims.
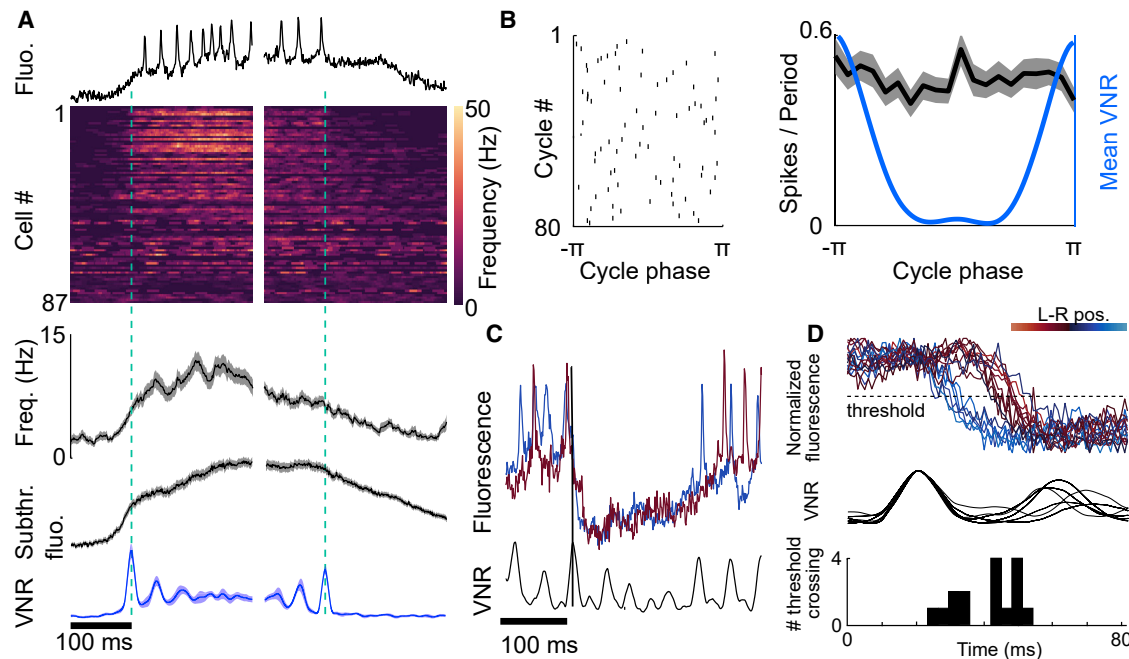
Figure 2. Voltage imaging characterization of V3 neurons

(A) Top: example V3 recording and spike rates of all V3 neurons aligned to start and end of swim bouts. Spike rate for each neuron was averaged over 5 to 25 bouts. Neurons sorted by bout activity index (*I*) (STAR Methods). Middle: grand average spike rates for all neurons and subthreshold fluorescence with spike computationally removed. Bottom: corresponding mean VNR signals aligned to start and end of swim bouts. Shaded area denotes SEM (n = 189 bouts).

(B) Left: spike raster plot of a single V3 neuron for 80 swim cycles. Spikes were uniformly distributed throughout the VNR phase. Right: VNR-triggered grand average spike rate of V3 neurons showing no phase-dependent modulation in spike rate. Shaded area denotes SEM (n = 87 cells).

(C) Rapid inhibition of two V3 neurons on the left (red) and right (blue) sides of the spinal cord during a swim bout.

(D) Top: mean fluorescence transient during midbout inhibitory events, aligned relative to preceding VNR peak and color coded according to the cell-body position on the left-right axis (n = 16 cells, 5–18 events per cell). Middle: corresponding mean VNR signal. Bottom: histogram of threshold crossings showing two-peaked distribution separated by half a VNR cycle. See also Figures S4 and S5.

We analyzed the subthreshold dynamics of the V3 neurons to determine whether they were driven by a single source or whether they comprised distinct subensembles. After digitally removing spikes, we found that the remaining subthreshold dynamics were strongly correlated across cells (Figure S5A). A principal-component analysis of simultaneously recorded V3 cells (n = 22 cells) found that 86% of the variance in the dataset could be accounted for by the first principal component (Figures S5B and S5C). These results suggest that the V3 population was primarily driven by a one-dimensional input.

A closer inspection of individual traces, however, revealed some distinctive dynamics in subsets of cells. V3 recordings showed occasional fast-membrane hyperpolarizations during swim bouts, indicative of inhibitory inputs to V3 (Figure 2C). Although V3 spiking and most subthreshold activity were not phase locked to motor rhythm, we noticed that for each cell the hyperpolarizations bore a definite phase relation to the VNR signal, which was constant across multiple events. Moreover, when comparing between cells, the phases of hyperpolarizing events separated into two clusters spaced by half a VNR cycle. These two clusters corresponded to V3 cell body position on the left and right side of the spinal cord (Figure 2D). Together, these observations imply that V3 neurons receive inputs from an inhibitory population that is phase locked to the VNR, is sporad-

ically active for one or two swim cycles, and synapses in a lateralized pattern.

High-speed recordings enabled mapping action-potential propagation within individual V3 neurons. We applied the sub-Nyquist action potential timing (SNAPT) technique, which had previously been used to map action-potential propagation in cultured neurons (Hochbaum et al., 2014) (STAR Methods). For each neuron, we extracted spike times from the fluorescence waveform at the soma. We calculated a spike-triggered average movie, typically averaging 100 to 300 spikes from a 25-s recording, and then fit a smoothing spline to the fluorescent trace along the axon and dendrites. This interpolated time trace allowed us to determine the average time lag of the spike peak at sub-frame-rate precision (Figure 3A). In recordings with high signal-to-noise ratio and neurites aligned with the focal plane, this analysis clearly showed action-potential initiation at or near the soma and propagation outward (Video S3). The average conduction velocity was 0.19 ± 0.07 m/s (mean ± SEM, n = 7 neurons) (Figures 3B and 3C), roughly two times the speed of the traveling wave in the more dorsal oscillatory population (Figure 1H) and similar to the conduction velocity recently reported for type I V2a neurons (Menelaou and McLean, 2019).

We then used the fact that distinct neurons rarely spiked at the same time (Figures S5D and S5E) to disentangle the signals
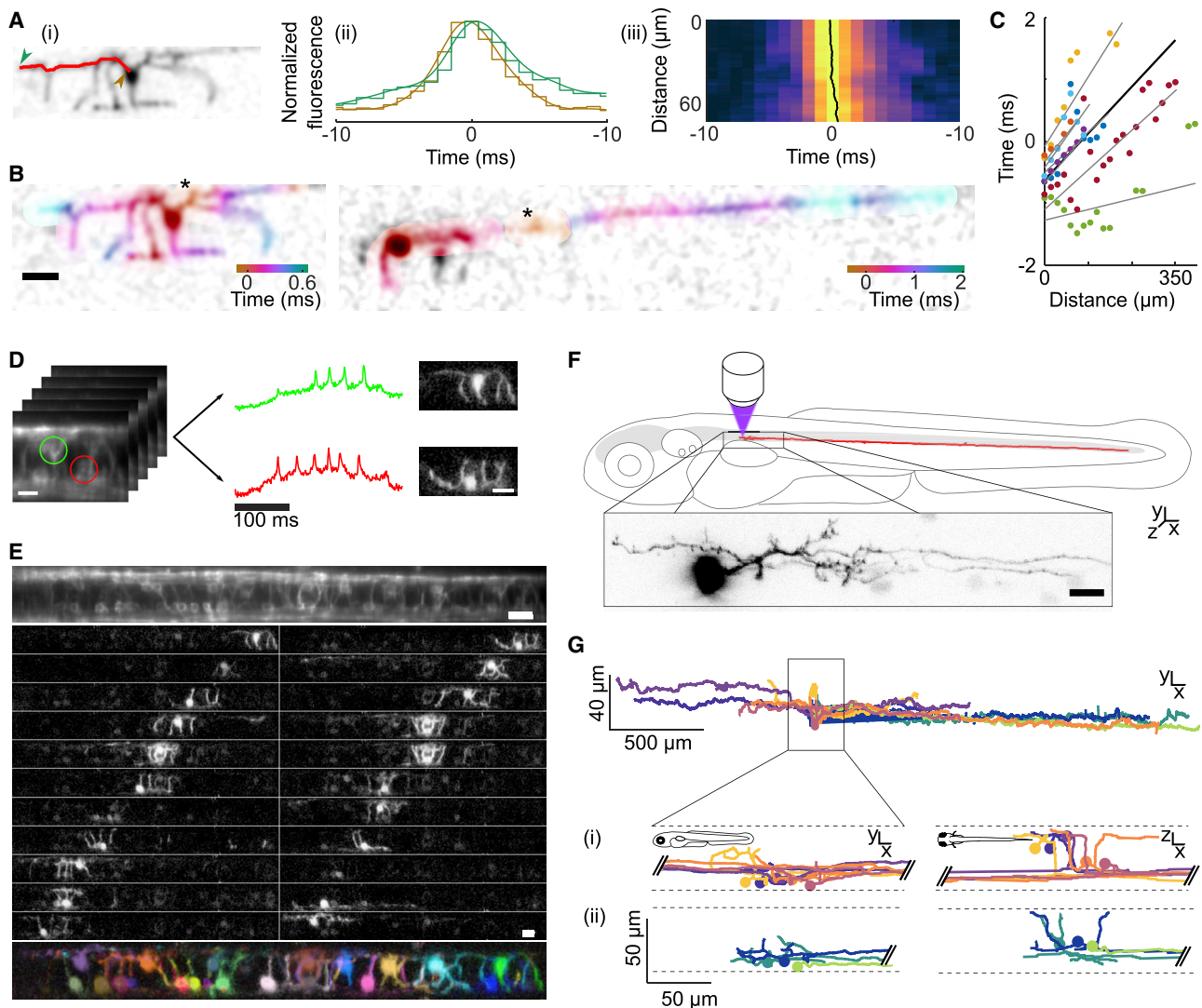
Figure 3. Action potential propagation and V3 morphology

(A) (i) Spatial footprint of a V3 neuron with one neurite marked in red. (ii) Spike-triggered average action potential waveform sampled at discrete 1-ms camera frames (staircase) and interpolated smooth waveforms, from the proximal (brown) and distal (green) ends of the neurite indicated in (i). (iii) Action potential propagation along the neurite marked in (i). Color indicates the normalized fluorescence. Black line indicates the sub-Nyquist interpolated peak timing.

(B) Action potential propagation along two neurons. Color denotes time delay; scale bar, 20 μm. Action potential initiation sites (black stars) are consistent with action potential initiation at the axon initial segment.

(C) Linear fits to the action potential propagation of seven neurons (gray lines) and the average fit (black line). Same colored dots are from the same neuron, each dot represents the binned value over 18 μm or neurite length. The mean conduction velocity was 0.19 ± 0.07 m/s (mean ± SEM).

(D) Schematic of activity-based segmentation. Voltage traces measured at the soma were used to calculate an average spike-triggered movie and spike waveform. Pixelwise correlation of the spike waveform and the video revealed the neuron morphology (STAR Methods). Scale bar, 10 μm.

(E) Top: average zArchon1 fluorescence from a voltage-imaging video (25,000 frames). Middle: map of spike-triggered average fluorescence amplitude for each neuron in the recording. Bottom: composite image with a different color for each functionally identified cell. Scale bar, 20 μm.

(F) Tracing of a photoconverted V3 neuron in the *Tg(vGlut2a:Gal4; UAS:Kaede)* line. Red line shows extent of the axon. Inset shows morphology near the soma. Scale bar, 10 μm.

(G) Top: morphology of photoconverted V3 neurons. Cell bodies were aligned relative to each other along the rostral-caudal axis and relative to the ventral margin of the spinal cord along the dorsoventral axis. Bottom: magnified region. Positions were shifted along rostral-caudal axis for better visualization. (i) V3 neurons with bifurcating axons. (ii) V3 neurons with descending axons. See also Figure S5.

from densely overlapping neurites. The spike-triggered average movies of each cell clearly showed electrical activation in the cell body and nearby axodendritic arbor, with little contamination from other cells. We calculated a pixelwise cross-correlation of the average spike waveform from each cell with the cell's spike-triggered average movie. This map revealed the morphology of the neurites around the cell body (Figure 3D). We computationally extracted the morphology of every neuron
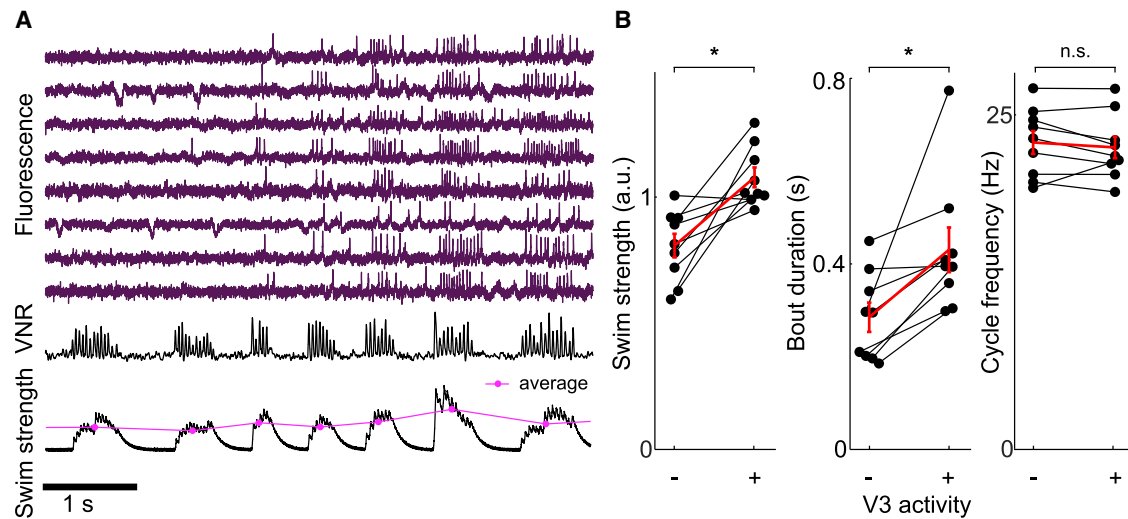
Figure 4. V3 activity correlates with increased swim strength

(A) Eight simultaneously recorded V3 neurons during swims of different strengths. All neurons increased firing during stronger swim bouts.

(B) V3 activity correlated with swim strength and bout duration, but not cycle frequency. Each dot represents the average of all bouts in each category from one field of view. Red line denotes average ± SEM. V3 activity was defined as >50% of V3 neurons in the field of view spiking at least once during the bout. N = 9 field of views from 7 fish. Significance threshold α = 0.017 after Bonferroni correction, paired t test.

and then re-created a composite image with the individual neurons identified (Figure 3E).

To explore the morphology of ventral glutamatergic neurons beyond the range accessible via functional unmixing, we tagged the arbors of individual cells using a photoconvertible fluorescent protein. We expressed the protein Kaede in glutamatergic neurons by driving expression of *Tg(UAS:Kaede)* in the *Tg(vGlut2a:Gal4)* line. Single cells were illuminated with a focused laser beam (405 nm), and then the photoconverted product was allowed to diffuse through the arbor for 24 h. The morphology from the dendrites around the cell body closely resembled that measured from the functional imaging data (Figure 3F), validating the activity-based morphological reconstructions.

We observed two morphological classes of ventral glutamatergic neurons, one with a long descending axon (3 of 8 cells) and a second one with a bifurcating axon (5 of 8 cells) (Figure 3A). Because of the continuous distribution of cell bodies along the left-right axis, it was not possible to determine unambiguously whether projections were mostly ipsilateral or contralateral. Axons spanned an average distance of 1.7 ± 0.5 mm (mean ± SD, n = 8 neurons) with bifurcating axons equally split between the descending and ascending parts (ascending: 0.6 ± 0.4 mm, descending: 0.5 ± 0.2 mm). Throughout their extent, the axons stayed at the ventral margin of the spinal cord (Figure 3B). The population with a descending axon has previously been described as VeMe cells (Hale et al., 2001). The bifurcating neurons represent a previously undescribed morphology. Given the prevalence of the bifurcating morphology (5 of 8 cells), it is unlikely that these neurons were entirely drawn from a non-V3 (≤24%) subpopulation. A potential target of the V3 axons are secondary motor neurons involved in slow swimming (Menelaou and McLean, 2012), suggesting a possible role for V3 neurons in modulating slow swimming.

V3 neuron activity modulates larval swim bouts during slow swimming

Because of their nonrhythmic spiking, V3 neurons are unlikely to be part of the central pattern generator (CPG) generating the swimming oscillations, yet their distinct firing during swim bouts suggested an acute relationship to locomotion. We hypothesized that V3 neurons might modulate locomotor output.

To test whether V3 activity associated with changes in motor output, we recorded V3 spiking activity while changing the feedback gain and the speed of the optic flow in our VR setup. This modulation caused V3 neurons to spike during some bouts but not others (Figure 4A). We measured average fictive swim strength (STAR Methods) as a function of V3 activity. Fish showed a 38% increase in swim strength during bouts with high V3 activity (as defined by >50% of neurons in the field of view showing spiking during the bout) compared with bouts with low V3 activity (swim strength, 1.07 ± 0.04 a.u. versus 0.81 ± 0.05 a.u.; mean ± SEM; p = 0.0041, paired t test; N = 9 fields of view from 7 fish) (Figure 4B). We also measured a 50% increase in bout duration in bouts with high versus low V3 activity (430 ± 48 ms versus 286 ± 31 ms; p = 0.0135). Remarkably, there was no difference in oscillation frequency between bouts where V3 neurons showed high versus low activity (22.6 ± 0.8 Hz versus 22.9 ± 0.9 Hz, mean ± SEM; p = 0.4, paired t test) (Figure 4B). This observation is in contrast to the activity of many other spinal interneurons whose firing correlates with tail beat frequency (Ampatzis et al., 2014; Kimura and Higashijima, 2019; McLean et al., 2007, 2008), suggesting a distinct role for V3 neurons.

We next sought to determine whether the correlation between V3 neuron spiking and bout strength was causal by optogenetically activating V3 neurons and measuring the effect on tail motions. To that end, we generated a transgenic line conditionally expressing channelrhodopsin (ChR) wide receiver
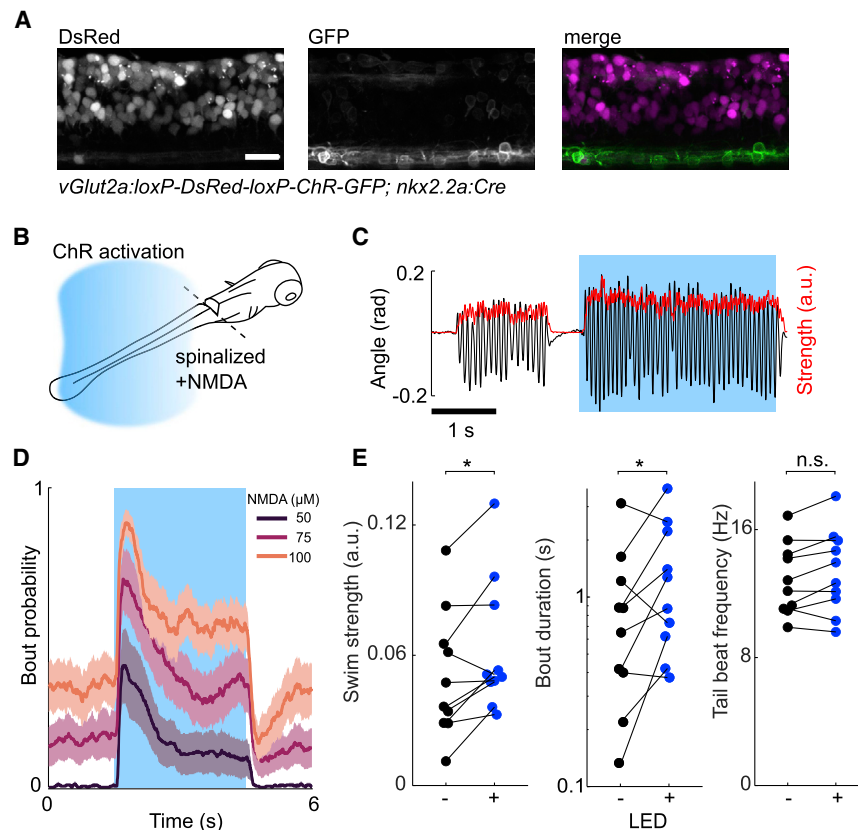
Neuron
Article

CellPress

Figure 5. Optogenetic activation of V3 neurons increases swim strength in spinalized larvae

(A) Lateral view of a spinal cord segment of *Tg(vGlut2a:loxP-DsRed-loxP-ChR-GFP; nkx2.2:Cre)* larva expressing ChR-GFP in V3 neurons. Scale bar, 20 μm.

(B) Schematic of the experimental setup.

(C) Spontaneous and optogenetically evoked tail oscillations in the presence of 100-μM NMDA. Blue indicates ChR stimulation.

(D) Average bout probability at increasing concentrations of NMDA during ChR stimulation (blue). N = 10 fish, averaged over 20 repetitions, shaded area denotes SEM.

(E) Optogenetic stimulation increased bout duration and swim strength, but not beat frequency. Experiments performed at 100-μM NMDA. For statistical model, see Table S1.

(Wang et al., 2009) in glutamatergic neurons (*Tg(vglut2a:loxP-DsRed-loxP-ChR-GFP)*) and a second line expressing Cre-recombinase in the ventral p3 domain (*Tg(nkx2.2b-Cre)*). This allowed us to express ChR only in V3 neurons (Figure 5A). To prevent possible visual artifacts during light stimulation and to uncouple the spinal cord circuits from upstream brain areas, we spinalized 5–6 dpf larvae and applied NMDA to the bath (Figures 5B and 5C). This protocol has been shown to induce rhythmic swim bouts and rests, although the tail beat frequency is lower than during swimming in an intact fish (Callahan et al., 2019; McDearmid and Drapeau, 2006).

Tonic optogenetic activation of V3 neurons led to an increase in the probability of starting a swim bout, in the duration of the swim bouts, and in the amplitude of the tail oscillations during NMDA-induced swim bouts (Figure 5D). Swim bouts often began immediately after the start of illumination, indicating that V3 activity was sufficient to initiate swimming. Swim bouts also often stopped immediately after the blue light was turned off. At 100-μM NMDA, optogenetic stimulation increased the bout duration (τ) (τ_{blue}/τ_{dark} = 2.0 ± 0.4, mean ± SEM; see STAR Methods for regression model and statistical testing), and also increased the swim strength (S) (S_{blue}/S_{dark} = 1.5 ± 0.2) (Figure 5E). In concordance with our data from fictive swimming, we did not observe a significant optogenetically induced change in tail beat frequency (F) (F_{blue}/F_{dark} = 1.04 ± 0.02).

Finally, we tested the effect of V3 activity on freely behaving larvae. We generated a conditional knockout line that expressed the cytotoxic peptide diphtheria toxin A (DTA) under the control of the *sim1a* promoter (*Tg(sim1a:loxP-DsRed-loxP-DTA)*), a marker of V3 neurons (Borowska et al., 2013). To selectively ablate V3 neurons in the spinal cord only, we crossed *Tg(sim1a:loxP-DsRed-loxP-DTA)* to the spinal-cord-specific Cre driver line *Tg(hox4a/9a:Cre)* (Kimura and Higashijima, 2019). We verified the ablation by backcrossing these fish to *Tg(vGlut2a:GFP)*, which showed a loss of ~85% of ventral glutamatergic neurons in the spinal cord in 5–6 dpf larvae (Figure 6A), consistent with our prior finding that most ventral glutamatergic neurons were V3. To induce different swimming speeds, we placed larvae in a 76.2- × 15.7-mm arena and elicited an optomotor response (OMR) by presenting a moving grating at different speeds while monitoring behavior with a high-speed camera (Figure 6B).

Larvae with V3 neurons ablated did not show any gross morphological or behavioral defects and initiated swim events at a slightly increased rate compared with control larvae (ablated: 0.78 ± 0.03 Hz, control: 0.63 ± 0.03 Hz; mean ± SEM; N = 28 ablated, 40 controls, p = 0.003, two-sample t test). We thus sought to determine whether there were subtle differences in swimming behaviors or kinematics, looking across several kinematic parameters (Figure S6). To compare the free-swimming behavior to our results from voltage imaging and optogenetic activation, we measured the swim speed per bout and duration for each bout at different grating speeds. We found that control larvae continually increased their swim speed with increasing OMR grating speed (slope: 0.51 ± 0.06, mean ± SEM), whereas V3 ablated larvae showed a reduced dependence of swim speed on OMR speed (slope: 0.17 ± 0.09, p = 0.0001) (see STAR Methods for details about the linear regression model). This finding indicates that V3 ablated larvae are less able to modulate their swim speed than are controls. Ablation of V3 neurons had no significant effect on bout duration (wild type: 175 ± 3 ms, knockout: 180 ± 4 ms) and very small effect on tail beat frequency (wild type: 21.1 ± 0.1 Hz, knockout: 21.6 ± 0.3 Hz) (Figure 6C).
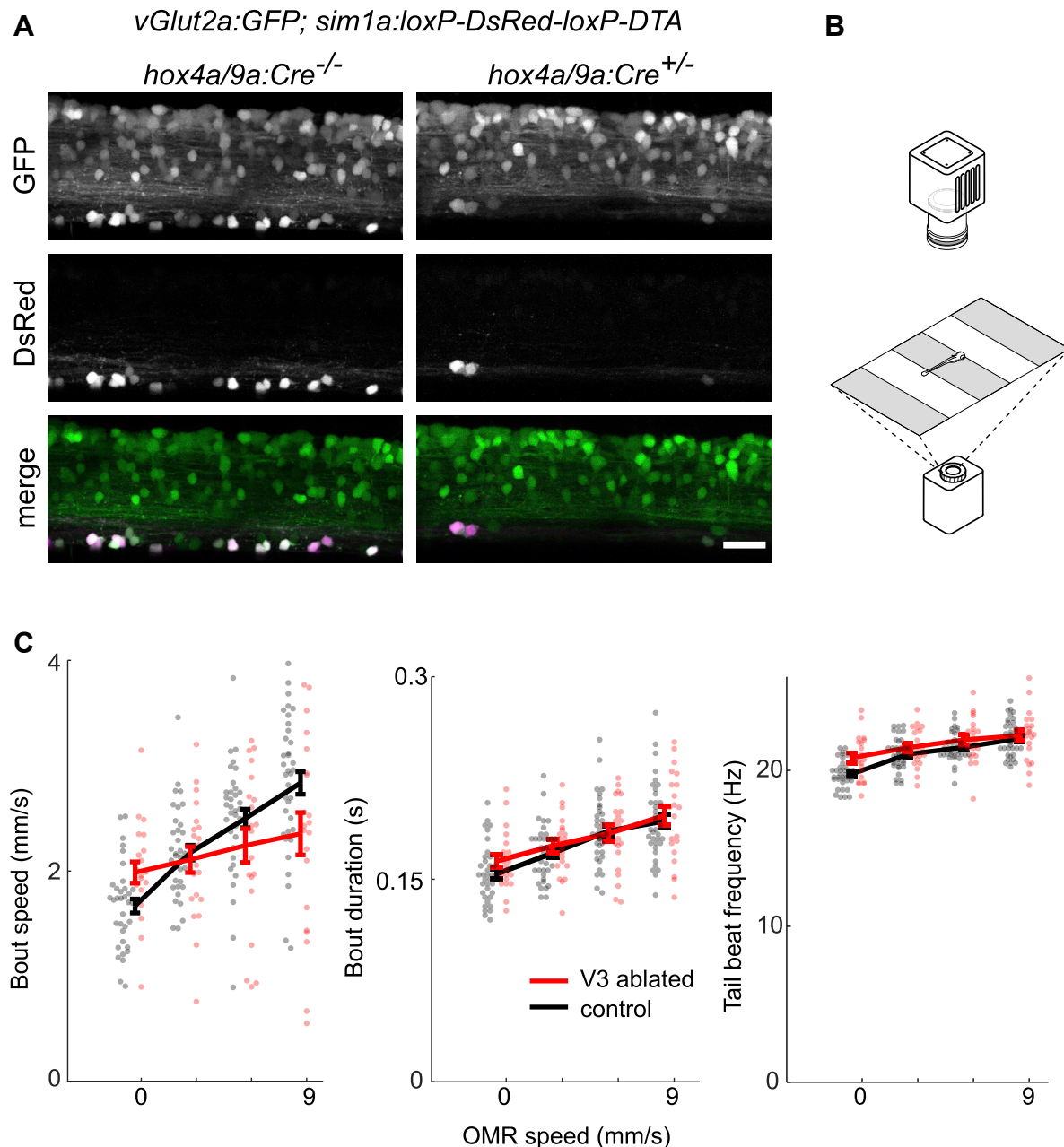
Figure 6. V3 neurons are necessary for swim speed adaptation

(A) Lateral view of the spinal cord of *Tg(vGlut2aGFP; sim1a:loxP-DsRed-loxP-DTA)* without (left panel) or with (right panel) *Tg(hox4a/9a:Cre)*. Cre expression led to the loss of most V3 neurons as seen from the absence of DsRed-expressing cells in the ventral spinal cord. Scale bar, 20 μm.

(B) Schematic of the behavioral testing setup. Free-swimming larvae were presented with a moving grating from below and recorded from above.

(C) V3-ablated larvae showed reduced modulation of bout speed in response to changes in OMR grating speed, but no difference in tail beat frequency or bout duration. Each dot represents the median value for one fish; the line represents e average value across fish; error bars: SEM. N = 28 ablated and 40 control fish. See also Figure S6. For the statistical model, see Table S2.

DISCUSSION

Voltage imaging for mapping neural dynamics in zebrafish spinal cord

Simultaneous voltage imaging from many neurons during behavior is a powerful method to characterize the repertoire of neural dynamics and to infer possible circuit mechanisms, but applications to dissecting circuit mechanisms remain sparse (Fan et al., 2020). By combining light-sheet voltage imaging and fictive behavior in a VR environment, we identified and characterized distinct functional subpopulations in the zebrafish spinal cord. Voltage imaging was an essential tool in our studies

because the underlying behaviors (tail oscillations) were far faster than Ca²⁺ imaging kinetics and because subthreshold potentials were a critical part of the analysis.

The zebrafish spinal cord is well suited to analysis by voltage imaging because its long and thin geometry coincides with the elongated camera field of view required for high-speed imaging; moreover, light-sheet microscopy provides optical sectioning *in vivo* for high sensitivity and good background rejection. Further, VNR recordings and a closed-loop VR environment permitted studies of naturalistic dynamics in a preparation where motion artifacts were minimal while still inducing naturalistic behavior. The VNR recording provided a means to synchronize activity measured at different focal planes, fields of view, and animals.

The primary limitation in our approach is that even with a 1-kHz recording rate, the very fast spikes of the dorsal oscillatory neurons were only detectable above noise in the most strongly expressing neurons. Further improvements in sensor speed, brightness, sensitivity, and expression are needed, along with improved high-speed imaging systems, to reliably study spiking in this population of neurons. In principle, the entire zebrafish spinal cord is accessible to light-sheet voltage imaging (our current field of view was mainly limited by the available laser power), and with advances in optics, it may become possible to record from a substantial fraction of the neurons simultaneously (Yoon et al., 2020; Zhang et al., 2021b).

Excitatory activity in the zebrafish spinal cord

We identified three main groups of glutamatergic neurons active during slow forward swimming: oscillating neurons, dorsal non-oscillating neurons, and ventral nonoscillating neurons. The oscillating neurons are most likely V0v and V2a neurons, which have been described as the major excitatory source that drives the CPG in the larval zebrafish (Ljunggren et al., 2014; McLean et al., 2007, 2008). V0v and V2a neurons have been shown to be recruited in a frequency-dependent manner, and V0v neurons are inhibited at higher swimming frequencies. Because our experiments mainly induced low-frequency swimming, we did not distinguish between these two classes in our analyses.

By measuring subthreshold membrane voltages, we mapped the phases of the oscillatory subpopulation across and along the spinal cord. Undulatory locomotion is generated by a linear phase gradient of motor activity and muscle contraction along the spinal cord (Grillner et al., 1993; Masino and Fetcho, 2005). Our recordings show a similar phase gradient and propagation of activity at the level of excitatory premotor interneurons.

A subset of the nonoscillatory dorsal neurons spiked between swim bouts and were silent during bouts (Figure S3). Sensory input is generally received in the dorsal part of the spinal cord. Sensory gating has been described for many sensory systems, including cutaneous touch input in zebrafish (Knogler and Drapeau, 2014). We speculate that these interbout-active neurons might receive sensory input that is shunted during movement. Our dataset provides a starting point to investigate the role of sensory input in spinal interneurons and their gating during behavior.

The ventral nonoscillating population comprises predominantly V3 neurons, at least 76% according to the co-expression

experiments (Figure S4) and at least 85% according to the genetic ablation experiments (Figure 6A). To our knowledge, V3 neurons are the first identified population of motor-related spinal cord neurons that fire tonically instead of being phase locked to the CPG. Nonoscillating activity might arise from tonic inputs from the brainstem but could also be due to receiving local out-of-phase excitation from both sides of the spinal cord. The occasional phase-locked inhibition we observed in V3 neurons suggests that they can be controlled with cycle-timing precision. Such inhibition might be necessary when performing fast corrective movements or when switching to a higher-frequency swim module midbout, which would require coordinated deactivation of the slow swim circuits. V1 inhibitory neurons have been shown to provide in-phase inhibition to silence slow motor neurons at higher frequencies and could be a source for phase-locked inhibition in V3 neurons (Kimura and Higashijima, 2019; Sengupta et al., 2021). Morphological reconstruction showed that there are at least two classes of ventral glutamatergic neurons that can be distinguished by their descending or bifurcating axon

Different morphological subtypes have also been described in the mouse spinal cord where a larger variety of V3 neurons exists (Blacklaws et al., 2015; Chopek et al., 2018; Zhang et al., 2008). Interestingly, while V3 neurons in adult mice predominantly consist of commissural neurons, a large fraction of V3 neurons are ipsilateral descending during embryonic development (Blacklaws et al., 2015). These neurons more closely resemble the descending neurons in zebrafish larva, and it is unknown whether more commissural types emerge in adult zebrafish.

V3 neurons as modulators of swim strength

Our experiments in free-swimming fish showed that V3 neurons are necessary for fish to track changes in OMR grating speed. Overall, the effect of V3 ablation on larval swimming was rather mild and not the precise opposite of the optogenetic activation experiments. The knockout animals may have compensated for the lack of V3 activity either by changes in motor commands during swimming or by changes in circuit properties during development. Neither of these mechanisms is possible in the spinalized preparation with optogenetic activation. Given that there are multiple examples of mirror effects in chronic versus acute manipulations (e.g., Cregg et al., 2020; Dougherty et al., 2013, but see also Otchy et al. 2015), we consider direct compensation of the motor signal the most likely reason for the mild knockout phenotype, though this hypothesis remains speculative. We also cannot rule out the possibility that a small population of non-V3 neurons contributed to the effect of optogenetic activation.

Our voltage-imaging and optogenetic experiments point to a V3 function that is not along the canonical frequency-speed axis (Callahan et al., 2019; Müller and van Leeuwen, 2004; Severi et al., 2014) but rather through the modulation of swim strength. A frequency-independent effect of V3 activity on motor neurons has also recently been suggested in a study using laser ablations of V3 neurons (Wiggin et al., 2021), suggesting that V3 neurons might modulate swim strength by acting on the recruitment of motor neurons. This observation suggests complementary modes of CPG modulation, corresponding approximately to frequency modulation and amplitude modulation, closely related to

the idea of independent pattern and rhythm generation. Amplitude modulation in mammals has been proposed to be mediated by last-order neurons (Kiehn, 2006), suggesting the hypothesis that V3 neurons may directly contact motor neurons in zebrafish, similar to what has been shown in mice (Chopek et al., 2018; Zhang et al., 2008). In zebrafish, frequency-independent amplitude modulation has also been reported via direct dopaminergic action on motor neurons during slow swimming (Jha and Thirumalai, 2020) and via subsets of V2a interneurons at higher cycle frequencies (Menelaou and McLean, 2019). Together, these results point to amplitude modulation as a general control motif, possibly implemented via several distinct mechanisms.

Although our optogenetic experiments showed that V3 activation was sufficient to trigger swim bouts (in the presence of NMDA), our fictive swimming and ablation experiments indicated that V3 activity is not necessary for swimming. Specifically, in the fictive swimming assays, low-strength swim bouts often occurred without firing any V3 neurons in the field of view (Figure 3), and in free-swimming fish lacking V3 neurons, the rate of bout initiation was actually slightly higher than in sibling controls. These observations suggest that V3 neurons are not a primary driver of bout initiation under physiological conditions but that they rather serve to modulate the power once a bout is initiated and perhaps to sustain ongoing bouts.

Experimental and modeling studies in adult mice showed that V3 neurons are important for synchronizing activity between left and right (Danner et al., 2019; Zhang et al., 2021a, 2008). V3 neurons also play a role in switching lumbar and cervical rhythm generators to higher speed gates; impairment of V3 function leads to slower locomotion (Danner et al., 2019; Zhang et al., 2008, 2021a). This result is qualitatively similar to our data where V3 knockouts had difficulty swimming at higher speeds, although a direct comparison is challenging because there are no comparable gate changes in zebrafish.

Although the *in vivo* recruitment pattern of V3 neurons in mice is not known, models of V3 activity assume rhythmic activity, which is phase locked to the spinal rhythm generators (Danner et al., 2019; Zhang et al., 2021a). Our data show that in larval zebrafish, V3 neurons are not rhythmically active, and therefore, a direct role in synchronization as proposed in mice is unlikely. It is plausible that V3 neurons serve different roles in quadruped versus axial locomotion and are therefore recruited differently in different species. There might also be a change in recruitment pattern over the course of development, a possibility that the zebrafish is well suited to address.

Larval zebrafish can show motor learning over several bouts to adjust their motor output to changing environmental conditions (Ahrens et al., 2012; Kawashima et al., 2016). The memory component of motor learning depends on serotonergic activity in the dorsal raphe nucleus, but the targets of the serotonergic modulation are not known. Our data suggest the hypothesis that serotonin may (directly or indirectly) modulate the gain of the spinal cord by acting on V3 neurons.

The tools and methods described here provide a unique window into spinal-circuit dynamics during (fictive) behaviors. Measurements *in vivo* are essential for identifying naturalistic firing patterns. These approaches are expected to generalize to other spinal sensory and motor populations.

STAR★METHODS

Detailed methods are provided in the online version of this paper and include the following:

- KEY RESOURCES TABLE
- RESOURCE AVAILABILITY
  - Lead contact
  - Materials availability
  - Data and code availability
- EXPERIMENTAL MODEL AND SUBJECT DETAILS
  - Zebrafish husbandry
- METHOD DETAILS
  - Zebrafish transgenesis
  - Imaging setup
  - Sample preparation
  - Electrophysiology
  - Closed-loop virtual environment
  - Data analysis
  - Sub-Nyquist action potential timing
  - Spike-based extraction of neuronal morphology
  - Kaede conversion and single-cell morphology
  - Channelrhodopsin stimulation
  - Free swimming experiments
- QUANTIFICATION AND STATISTICAL ANALYSIS
  - ChR activation experiments
  - Free swimming experiments

SUPPLEMENTAL INFORMATION

Supplemental information can be found online at https://doi.org/10.1016/j.neuron.2022.01.001.

AUTHOR CONTRIBUTIONS

Conceptualization, U.L.B. and A.E.C.; methodology, U.L.B. and A.E.C.; software, U.L.B.; investigation, U.L.B.; resources, Y.K., T.K., S.-i.H., and M.B.A.; writing – original draft, U.L.B. and A.E.C.; writing – review & editing, U.L.B., A.E.C., T.K., F.E., S.-i.H., and M.B.A.; supervision, A.E.C. and F.E.; funding acquisition, A.E.C.

DECLARATION OF INTERESTS

The authors declare no competing interests.

Neuron
Article

CellPress

REFERENCES

Abdelfattah, A.S., Kawashima, T., Singh, A., Novak, O., Liu, H., Shuai, Y., Huang, Y.-C., Campagnola, L., Seeman, S.C., Yu, J., et al. (2019). Bright and photostable chemigenetic indicators for extended in vivo voltage imaging. Science *365*, 699–704.

Adam, Y., Kim, J.J., Lou, S., Zhao, Y., Xie, M.E., Brinks, D., Wu, H., Mostajo-Radji, M.A., Kheifets, S., Parot, V., et al. (2019). Voltage imaging and optogenetics reveal behaviour-dependent changes in hippocampal dynamics. Nature *569*, 413–417.

Ahrens, M.B., Huang, K.H., Narayan, S., Mensh, B.D., and Engert, F. (2013). Two-photon calcium imaging during fictive navigation in virtual environments. Front. Neural Circuits *7*, 104.

Ahrens, M.B., Li, J.M., Orger, M.B., Robson, D.N., Schier, A.F., Engert, F., and Portugues, R. (2012). Brain-wide neuronal dynamics during motor adaptation in zebrafish. Nature *485*, 471–477.

Ampatzis, K., Song, J., Ausborn, J., and El Manira, A. (2014). Separate microcircuit modules of distinct v2a interneurons and motoneurons control the speed of locomotion. Neuron *83*, 934–943.

Blacklaws, J., Deska-Gauthier, D., Jones, C.T., Petracca, Y.L., Liu, M., Zhang, H., Fawcett, J.P., Glover, J.C., Lanuza, G.M., and Zhang, Y. (2015). Sim1 is required for the migration and axonal projections of V3 interneurons in the developing mouse spinal cord. Dev. Neurobiol. *75*, 1003–1017.

Borowska, J., Jones, C.T., Zhang, H., Blacklaws, J., Goulding, M., and Zhang, Y. (2013). Functional subpopulations of V3 interneurons in the mature mouse spinal cord. J. Neurosci. *33*, 18553–18565.

Bruno, A.M., Frost, W.N., and Humphries, M.D. (2015). Modular deconstruction reveals the dynamical and physical building blocks of a locomotion motor program. Neuron *86*, 304–318.

Budick, S.A., and O'Malley, D.M. (2000). Locomotor repertoire of the larval zebrafish: swimming, turning and prey capture. J. Exp. Biol. *203*, 2565–2579.

Buss, R.R., and Drapeau, P. (2001). Synaptic drive to motoneurons during fictive swimming in the developing zebrafish. J. Neurophysiol. *86*, 197–210.

Cai, C., Friedrich, J., Singh, A., Eybposh, M.H., Pnevmatikakis, E.A., Podgorski, K., and Giovannucci, A. (2021). VolPy: Automated and scalable analysis pipelines for voltage imaging datasets. PLoS Comput. Biol. *17*, e1008806.

Callahan, R.A., Roberts, R., SenGupta, M., Kimura, Y., Higashijima, S.I., and Bagnall, M.W. (2019). Spinal V2b neurons reveal a role for ipsilateral inhibition in speed control. eLife *8*, e47837.

Chien, M.-P., Brinks, D., Testa-Silva, G., Tian, H., Phil Brooks, F., Adam, Y., Bloxham, W., Gmeiner, B., Kheifets, S., and Cohen, A.E. (2021). Photoactivated voltage imaging in tissue with an archaerhodopsin-derived reporter. Sci. Adv. *7*, eabe3216.

Chopek, J.W., Nascimento, F., Beato, M., Brownstone, R.M., and Zhang, Y. (2018). Sub-populations of spinal V3 interneurons form focal modules of layered pre-motor microcircuits. Cell Rep *25*, 146–156.e3.

Cregg, J.M., Leiras, R., Montalant, A., Wanken, P., Wickersham, I.R., and Kiehn, O. (2020). Brainstem neurons that command mammalian locomotor asymmetries. Nat. Neurosci. *23*, 730–740.

Danner, S.M., Zhang, H., Shevtsova, N.A., Borowska-Fielding, J., Deska-Gauthier, D., Rybak, I.A., and Zhang, Y. (2019). Spinal V3 interneurons and left–right coordination in mammalian locomotion. Front. Cell. Neurosci. *13*, 516.

Dougherty, K.J., Zagoraiou, L., Satoh, D., Rozani, I., Doobar, S., Arber, S., Jessell, T.M., and Kiehn, O. (2013). Locomotor rhythm generation linked to the output of spinal shox2 excitatory interneurons. Neuron *80*, 920–933.

Fan, L.Z., Kheifets, S., Böhm, U.L., Wu, H., Piatkevich, K.D., Xie, M.E., Parot, V., Ha, Y., Evans, K.E., Boyden, E.S., et al. (2020). All-optical electrophysiology reveals the role of lateral inhibition in sensory processing in cortical layer 1. Cell *180*, 521–535.e18.

Gong, Y., Huang, C., Li, J.Z., Grewe, B.F., Zhang, Y., Eismann, S., and Schnitzer, M.J. (2015). High-speed recording of neural spikes in awake mice and flies with a fluorescent voltage sensor. Science *350*, 1361–1366.

Goulding, M. (2009). Circuits controlling vertebrate locomotion: Moving in a new direction. Nat. Rev. Neurosci. *10*, 507–518.

Grillner, S., and El Manira, A.E. (2015). The intrinsic operation of the networks that make us locomote. Curr. Opin. Neurobiol. *31*, 244–249.

Grillner, S., Matsushima, T., Wadden, T., Tegnér, J., El Manira, A., and Wallén, P. (1993). The neurophysiological bases of undulatory locomotion in vertebrates. Semin. Neurosci. *5*, 17–27.

Hale, M.E., Ritter, D.A., and Fetcho, J.R. (2001). A confocal study of spinal interneurons in living larval zebrafish. J. Comp. Neurol. *437*, 1–16.

Hatta, K., Tsujii, H., and Omura, T. (2006). Cell tracking using a photoconvertible fluorescent protein. Nat. Protoc. *1*, 960–967.

Higashijima, S.-I., Schaefer, M., and Fetcho, J.R. (2004). Neurotransmitter properties of spinal interneurons in embryonic and larval zebrafish. J. Comp. Neurol. *480*, 19–37.

Hochbaum, D.R., Zhao, Y., Farhi, S.L., Klapoetke, N., Werley, C.A., Kapoor, V., Zou, P., Kralj, J.M., Maclaurin, D., Smedemark-Margulies, N., et al. (2014). All-optical electrophysiology in mammalian neurons using engineered microbial rhodopsins. Nat. Methods *11*, 825–833.

Jha, U., and Thirumalai, V. (2020). Neuromodulatory selection of motor neuron recruitment patterns in a visuomotor behavior increases speed. Curr. Biol. *30*, 788–801.e3.

Kawashima, T., Zwart, M.F., Yang, C.-T., Mensh, B.D., and Ahrens, M.B. (2016). The serotonergic system tracks the outcomes of actions to mediate short-term motor learning. Cell *167*, 933–946.e20.

Kiehn, O. (2006). Locomotor circuits in the mammalian spinal cord. Annu. Rev. Neurosci. *29*, 279–306.

Kimura, Y., and Higashijima, S.-I. (2019). Regulation of locomotor speed and selection of active sets of neurons by V1 neurons. Nat. Commun. *10*, 2268.

Kimura, Y., Hisano, Y., Kawahara, A., and Higashijima, S.-i. (2014). Efficient generation of knock-in transgenic zebrafish carrying reporter/driver genes by CRISPR/Cas9-mediated genome engineering. Sci. Rep. *4*, 6545.

Kimura, Y., Okamura, Y., and Higashijima, S.-i. (2006). alx, a zebrafish homolog of Chx10, marks ipsilateral descending excitatory interneurons that participate in the regulation of spinal locomotor circuits. J. Neurosci. *26*, 5684–5697.

Knogler, L.D., and Drapeau, P. (2014). Sensory gating of an embryonic zebrafish interneuron during spontaneous motor behaviors. Front. Neural Circuits *8*, 121.

Ljunggren, E.E., Haupt, S., Ausborn, J., Ampatzis, K., and El Manira, A. (2014). Optogenetic activation of excitatory premotor interneurons is sufficient to generate coordinated locomotor activity in larval zebrafish. J. Neurosci. *34*, 134–139.

Longair, M.H., Baker, D.A., and Armstrong, J.D. (2011). Simple Neurite Tracer: open source software for reconstruction, visualization and analysis of neuronal processes. Bioinformatics *27*, 2453–2454.

Marques, J.C., Lackner, S., Félix, R., and Orger, M.B. (2018). Structure of the zebrafish locomotor repertoire revealed with unsupervised behavioral clustering. Curr. Biol. *28*, 181–195.e5.

Masino, M.A., and Fetcho, J.R. (2005). Fictive swimming motor patterns in wild type and mutant larval zebrafish. J. Neurophysiol. *93*, 3177–3188.

McDearmid, J.R., and Drapeau, P. (2006). Rhythmic motor activity evoked by NMDA in the spinal zebrafish larva. J. Neurophysiol. *95*, 401–417.

McLean, D.L., Fan, J., Higashijima, S.-i., Hale, M.E., and Fetcho, J.R. (2007). A topographic map of recruitment in spinal cord. Nature *446*, 71–75.

McLean, D.L., Masino, M.A., Koh, I.Y.Y., Lindquist, W.B., and Fetcho, J.R. (2008). Continuous shifts in the active set of spinal interneurons during changes in locomotor speed. Nat. Neurosci. *11*, 1419–1429.

Menelaou, E., and McLean, D.L. (2012). A gradient in endogenous rhythmicity and oscillatory drive matches recruitment order in an axial motor pool. J. Neurosci. *32*, 10925–10939.

Menelaou, E., and McLean, D.L. (2019). Hierarchical control of locomotion by distinct types of spinal V2a interneurons in zebrafish. Nat. Commun. *10*, 4197.

Müller, U.K., and van Leeuwen, J.L. (2004). Swimming of larval zebrafish: ontogeny of body waves and implications for locomotory development. J. Exp. Biol. *207*, 853–868.

Otchy, T.M., Wolff, S.B.E., Rhee, J.Y., Pehlevan, C., Kawai, R., Kempf, A., Gobes, S.M.H., and Ölveczky, B.P. (2015). Acute off-target effects of neural circuit manipulations. Nature *528*, 358–363.

Piatkevich, K.D., Bensussen, S., Tseng, H.-A., Shroff, S.N., Lopez-Huerta, V.G., Park, D., Jung, E.E., Shemesh, O.A., Straub, C., Gritton, H.J., et al. (2019). Population imaging of neural activity in awake behaving mice. Nature *574*, 413–417.

Piatkevich, K.D., Jung, E.E., Straub, C., Linghu, C., Park, D., Suk, H.-J., Hochbaum, D.R., Goodwin, D., Pnevmatikakis, E., Pak, N., et al. (2018). A robotic multidimensional directed evolution approach applied to fluorescent voltage reporters. Nat. Chem. Biol. *14*, 352–360.

Portugues, R., and Engert, F. (2011). Adaptive locomotor behavior in larval zebrafish. Front. Syst. Neurosci. *5*, 72.

Satou, C., Kimura, Y., and Higashijima, S.-i. (2012). Generation of multiple classes of V0 neurons in zebrafish spinal cord: progenitor heterogeneity and temporal control of neuronal diversity. J. Neurosci. *32*, 1771–1783.

Satou, C., Kimura, Y., Hirata, H., Suster, M.L., Kawakami, K., and Higashijima, S.-i. (2013). Transgenic tools to characterize neuronal properties of discrete populations of zebrafish neurons. Development *140*, 3927–3931.

SenGupta, M., Daliparthi, V., Roussel, Y., Bui, T.V., and Bagnall, M.W. (2021). Spinal V1 neurons inhibit motor targets locally and sensory targets distally. Curr. Biol. *31*, 3820–3833.e4.

Severi, K.E., Portugues, R., Marques, J.C., O'Malley, D.M., Orger, M.B., and Engert, F. (2014). Neural control and modulation of swimming speed in the larval zebrafish. Neuron *83*, 692–707.

Štih, V., Petrucco, L., Kist, A.M., and Portugues, R. (2019). Stytra: An open-source, integrated system for stimulation, tracking and closed-loop behavioral experiments. PLoS Comput. Biol. *15*, e1006699.

Tomina, Y., and Wagenaar, D.A. (2017). A double-sided microscope to realize whole-ganglion imaging of membrane potential in the medicinal leech. Elife *6*, e29839.

Umeda, K., Shoji, W., Sakai, S., Muto, A., Kawakami, K., Ishizuka, T., and Yawo, H. (2013). Targeted expression of a chimeric channelrhodopsin in zebrafish under regulation of Gal4-UAS system. Neurosci. Res. *75*, 69–75.

Villette, V., Chavarha, M., Dimov, I.K., Bradley, J., Pradhan, L., Mathieu, B., Evans, S.W., Chamberland, S., Shi, D., Yang, R., et al. (2019). Ultrafast two-photon imaging of a high-gain voltage indicator in awake behaving mice. Cell *179*, 1590–1608.e23.

Vladimirov, N., Mu, Y., Kawashima, T., Bennett, D.V., Yang, C.-T., Looger, L.L., Keller, P.J., Freeman, J., and Ahrens, M.B. (2014). Light-sheet functional imaging in fictively behaving zebrafish. Nat. Methods *11*, 883–884.

Wahlstrom-Helgren, S., Montgomery, J.E., Vanpelt, K.T., Biltz, S.L., Peck, J.H., and Masino, M.A. (2019). Glutamate receptor subtypes differentially contribute to optogenetically activated swimming in spinally transected zebrafish larvae. J. Neurophysiol. *122*, 2414–2426.

Wang, H., Sugiyama, Y., Hikima, T., Sugano, E., Tomita, H., Takahashi, T., Ishizuka, T., and Yawo, H. (2009). Molecular determinants differentiating photocurrent properties of two channelrhodopsins from chlamydomonas. J. Biol. Chem. *284*, 5685–5696.

Wiggin, T.D., Montgomery, J.E., Brunick, A.J., Peck, J.H., and Masino, M.A. (2021). V3 interneurons regulate locomotor vigor by recruitment of spinal motor neurons during fictive swimming in larval zebrafish. bioRxiv. https://doi.org/10.1101/2021.03.03.433646.

Xie, M.E., Adam, Y., Fan, L.Z., Böhm, U.L., Kinsella, I., Zhou, D., Rozsa, M., Singh, A., Svoboda, K., Paninski, L., and Cohen, A.E. (2021). High-fidelity estimates of spikes and subthreshold waveforms from 1-photon voltage imaging in vivo. Cell Rep *35*, 108954.

Yang, L., Rastegar, S., and Strähle, U. (2010). Regulatory interactions specifying Kolmer-Agduhr interneurons. Development *137*, 2713–2722.

Yoon, Y.-G., Wang, Z., Pak, N., Park, D., Dai, P., Kang, J.S., Suk, H.-J., Symvoulidis, P., Guner-Ataman, B., Wang, K., and Boyden, E.S. (2020). Sparse decomposition light-field microscopy for high speed imaging of neuronal activity. Optica *7*, 1457–1468.

Zhang, H., Shevtsova, N.A., Deska-Gauthier, D., Mackay, C., Dougherty, K.J., Danner, S.M., Zhang, Y., and Rybak, I.A. (2021a). The role of V3 neurons in speed-dependent interlimb coordination during locomotion in mice. bioRxiv. https://doi.org/10.1101/2021.09.01.458603.

Zhang, Y., Narayan, S., Geiman, E., Lanuza, G.M., Velasquez, T., Shanks, B., Akay, T., Dyck, J., Pearson, K., Gosgnach, S., et al. (2008). V3 spinal neurons establish a robust and balanced locomotor rhythm during walking. Neuron *60*, 84–96.

Zhang, Z., Bai, L., Cong, L., Yu, P., Zhang, T., Shi, W., Li, F., Du, J., and Wang, K. (2021b). Imaging volumetric dynamics at high speed in mouse and zebrafish brain with confocal light field microscopy. Nat. Biotechnol. *39*, 74–83.

Neuron
Article

 CellPress

STAR★METHODS

KEY RESOURCES TABLE

REAGENT or RESOURCE	SOURCE	IDENTIFIER
Deposited data		
Voltage imaging data	This study	DOI: 10.5281/zenodo.5792258
ChR activation data	This study	DOI: 10.5281/zenodo.5792258
Free swimming data	This study	DOI: 10.5281/zenodo.5792258
Experimental models: Organisms/strains		
Tg(vGlut2a:Gal4)	Satou et al., 2013	https://shigen.nig.ac.jp/zebrafish/strainDetailAction.do?strainId=435
Tg(UAS:zArchon1-GFP)	This study	N/A
Tg(vglut2a:loxP-DsRed-loxP-ChR-GFP)	This study	N/A
Tg(nkx2.2b-Cre)	This study	N/A
Tg(sim1a:loxP-DsRed-loxP-DTA)	This study	N/A
Tg(hox4a/9a:Cre)	Kimura and Higashijima, 2019	N/A
Tg(UAS:Kaede)	Hatta et al., 2006	ZFIN: rk8Tg
Tg(vGlut2a:GFP)	Satou et al., 2012	https://shigen.nig.ac.jp/zebrafish/strainDetailAction.do?strainId=340
Recombinant DNA		
pTol2-UAS-zArchon1-KGC-EGFP-ER2	Piatkevich et al., 2019	Addgene plasmid #108427
Software and algorithms		
Simple neurite tracer	Longair et al., 2011	https://imagej.net/plugins/snt/
Custom analysis pipeline	This study	DOI: 10.52 81/zenodo.5794540

RESOURCE AVAILABILITY

Lead contact
Further information and requests for resources and reagents should be directed to and will be fulfilled by the lead contact, Adam E. Cohen (cohen@chemistry.harvard.edu).

Materials availability
Fish lines are available through the National BioResource Project (https://shigen.nig.ac.jp/zebra/index_en.html) or through the lead contact.

Data and code availability
- Processed voltage imaging and behavior data have been deposited as Matlab data files at Zenodo and are publicly available as of the date of publication. DOIs are listed in the key resources table.
- All raw data reported in this paper will be shared by the lead contact upon request.
- All original code has been deposited at Zenodo and is publicly available as of the date of publication. DOIs are listed in the key resources table.
- Any additional information required to reanalyze the data reported in this paper is available from the lead contact upon request.

EXPERIMENTAL MODEL AND SUBJECT DETAILS

Zebrafish husbandry
All zebrafish experiments were approved by the Harvard University Institutional Animal Care and Use Committee (IACUC). All larvae were kept at a 10 h dark, 14 h light cycle at 28 °C until at least 5 dpf. Larval sex is not specified at this developmental stage and was therefore not determined.

A list of transgenic lines is included in the key resources table.

METHOD DETAILS

Zebrafish transgenesis

Tg(vglut2a:loxP-DsRed-loxP-ChR-GFP) fish were generated using the bacterial artificial chromosome (BAC) zK145P24 as described (Kimura et al., 2006). The loxP-DsRed-loxP-ChR-GFP DNA construct was generated using the loxP-DsRed-loxP-GFP construct: GFP was replaced with ChR-WideReceiver (Wang et al., 2009). *Tg(nkx2.2b:Cre)* fish were generated using the BAC transgenic method with BAC zKP50F5. The Cre DNA construct was described in Satou et al. (2012). *Tg(sim1a:loxP-DsRed-loxP-DTA)* fish were established using the CRISPR/Cas9 knock-in method (Kimura et al., 2014) with the DNA construct described in Kimura and Higashijima (2019). The insertion site was set upstream of the sim1a gene with the CRISPR target sequence: GAAGCGG CCGCCGGTGAATGGG.

The *Tg(UAS:zArchon1-KGC-GFP-ER2)* line was generated using the Tol2 transposon system. The plasmid (Piatkevich et al., 2018) and tol2 mRNA were injected in 2-cell stage embryos. We crossed the injected fish with a Gal4 line to screen for the expression of green fluorescence in the brain at the F1 generation.

Imaging setup

All voltage imaging data were acquired on a custom-built light sheet microscope (Figure S1). Output of an 800 mW 639 nm laser (MLL-FN-639, CNI Laser) was first expanded 2x isotropically and then stretched 2x along the x-axis using an anamorphic prism pair (PS875-A, Thorlabs). The light sheet was created using a 50 mm cylindrical lens focusing along the x-axis and reimaged onto the back focal plane of a 4x long working-distance objective (Olympus XLFluor4X/340, NA 0.28) using a scan lens (50 mm, AC254-050-A-ML, Thorlabs) and tube lens (150 mm, AC508-150-A-ML, Thorlabs). Nominal specifications for the sheet are: Rayleigh length: 46 μm, sheet thickness at focus 6.1 μm, sheet width 708 μm (all values as $1/e^2$). A galvo mirror at focal distance from the scan lens allowed moving the light sheet along the z-axis. The focal plane of the imaging objective was synchronously adjusted by moving the imaging objective with a piezo actuator (PIFOC, PD72Z4CA0).

Fluorescence was acquired through a 25x objective (Olympus XPlan N 25x WMP, NA 1.05) and a 100 mm tube lens (Thorlabs TTL-100 A), resulting in an effective magnification of 13.9x. Emission light was filtered using a 664 nm long-pass filter and images were acquired on sCMOS camera (Hamamatsu, Orca Flash4) at 996.3 frames/s. Typical illumination powers were 290 mW.

Three or four z-positions were recorded per x,y-position along the tail. At the end each recording a z-stack of the zArchon1 fluorescence across the entire depth of the spinal cord was recorded to reference each recorded neuron to anatomical coordinates in the spinal cord. The zArchon1-GFP expression pattern in Figure 1B was recorded with a custom-built two-photon excitation arm build on the same microscope.

Sample preparation

Zebrafish embryos at 5-7 days post fertilization (dpf) were paralyzed by immersing in 1 mg/ml alpha-bungarotoxin for 1-2 minutes before mounting in 1.5% low melting point agarose on a custom-built sample holder. For ventral nerve root (VNR) recordings the agarose was removed around a few segments of the tail. The sample holder together with the electrophysiology head stage was mounted on a x-y stage holding the larva inside a stationary sample chamber containing standard fish water. The larva and electrophysiology head stage can be moved together independently of the sample chamber. This design allowed to keep the sample chamber at a fixed distance from the light-sheet objective to avoid changes in the focal plane of the light when repositioning the sample (Figure S1).

Electrophysiology

VNR recordings were performed as previously described (Masino and Fetcho, 2005). Recording pipettes were pulled from glass capillaries (1B150F-4, WPI) to have a ~20 μm opening, filled with standard fish water and attached to the side of the larva by gentle suction. Data were acquired in current clamp mode using an Axon 200-B or 700-B patch clamp amplifier (Molecular Devices). The signal was low-pass filtered at 1 kHz, passed through a denoising filter to remove line noise (HumBug, Quest Scientific) and digitized at 50 kHz using custom written LabView code.

Closed-loop virtual environment

Larvae were presented with a forward moving square grating (grating period: 2 cm, moving speed 9.9 mm/s, fish position ~2 cm above the screen) using a video projector (Epson VS240). The light from the projector was filtered with a bandpass filter (575/40 nm) to prevent bleed-through of the projector light into the imaging channel, demagnified (f_{L1} = 200 mm) and projected onto white paper placed below the fish.

To provide closed-loop visual feedback from fictive swimming activity, we adapted the approach described in Ahrens et al. (2012) and implemented the online feedback on a microcontroller (Teensy 3.6, PJRC). The ventral nerve root signal was sampled at 10 kHz and filtered by subtracting an exponential moving average (α = 0.005/sample). The resulting high-pass filtered signal was used to calculate the standard deviation over a moving window of 10 ms. Signals that crossed a threshold value were assigned as swim events. To calculate the swimming strength, signal values exceeding the threshold were summed over time and filtered through a high-pass filter with a time constant of 100 ms. The output of the microcontroller was sent to LabView code which applied

Neuron
Article

CellPress

a user-defined gain and then subtracted the scaled motion signal from the constant forward speed of the grating and generated the video output for the projector. The feedback loop ran at a rate of 100 Hz, above the video projector refresh rate (60 Hz).

To calculate the final speed signal, for each fish a constant gain scale-factor was selected so that it could follow the grating at speeds of 9.9-15.1 mm/s and at variable gain of 0.5-1.5. Four consecutive 25 s recordings of the same field of view were recorded while changing the feedback gain from 0.5 to 1.5 or the grating speed from 9.9 mm/s to 15.1 mm/s. Grating speed was kept at 0 for the first 5 s of the recording.

Data analysis
VNR recordings
VNR recordings were band-pass filtered between 300 and 1000 Hz and the standard deviation over a moving 10 ms window followed by a moving average of the same window length was used to calculate the swim signal.

Fluorescence recordings
Using the average intensity image as a guide, masks were manually drawn around each soma in the field of view. Each frame was filtered with a median filter of 3x3 pixel and the fluorescence time-series at each pixel was high-pass filtered by subtracting a sliding median over a 201 ms window. Then PCA/ICA was performed on each cell body individually. The resulting components were inspected manually and one component per cell body was kept if it showed activity during the recording. The final fluorescence signal was calculated as $\Delta F/F = (F_{ICA}(t) - mean(F_{ICA}))/mean(F_{ICA})$.

To calculate the cycle-triggered average fluorescence waveform, the fluorescence was triggered on each VNR burst with a period in the range of 25 ms to 66.7 ms (14 Hz – 40 Hz). To average over cycles with different periods, individual cycles were linearly interpolated to have the same number of samples. The cycle amplitude was then calculated as the difference between the minimum and maximum value of the cycle-triggered average.

To analyze the phase relationships of oscillating neurons, only neurons with an average cycle amplitude $\geq$ 0.5 $\Delta F/F$ were included. To correct for apparent phase offsets between fish due to different placements of the VNR electrode, the average phase shift of all recorded cells in each field of view was set to 0.

Non-oscillating cells were defined as cells with a cycle triggered average amplitude < 0.5 $\Delta F/F$. Only non-oscillating cells were present in the ventral spinal cord. V3 neurons were thus defined as having a cell body position in the lower 30% of the spinal cord. To quantify the difference in spike rate during vs between bouts, a bout activity index was defined as

$$I = (SR_{bout} - SR_{interbout})/(SR_{bout} + SR_{interbout})$$

where SR is the spike rate. Only V3 neurons with $I > 0$ were included in the analysis.

Sub-Nyquist action potential timing
The calculation of the action potential delay along the neurite was adapted from Hochbaum et al. (2014). We first calculated the spike triggered average movie of each cell. Due to the rolling shutter of the sCMOS camera, this movie contained a time delay of 9.74436 μs between successive rows of pixels. We used digital interpolation to correct for this time delay. We used the spatial footprint of the neuron (see below) to trace the neurites of each neuron. We then calculated the spike waveform along the neurite by averaging the pixel values from successive 1 pixel long and 8 pixel wide regions. The resulting matrix (distance x time) was then filtered with a moving average of 40 pixels along the distance axis and a smoothing spline was fitted at each distance along the time axis (Matlab fit method 'SmoothingSpline', smoothing parameter 0.6). The position of the peak of the resulting function was considered the timing of the action potential maximum. For the analysis of action potential propagation, we measured the time delay along the longest neurite in the field of view from the 7 neurons that showed the strongest signal.

Spike-based extraction of neuronal morphology
To visualize the morphology of individual V3 neurons from the voltage imaging data, we generated spike triggered average movies and the corresponding spike triggered average fluorescence trace. We then calculated the correlation coefficient of the timeseries of each pixel and the average spike waveform. The resulting image was filtered with a 2D median filter with a radius of 2 pixels to remove noise. This approach gave an image of the single cell body and proximal neurites.

Kaede conversion and single-cell morphology
The Kaede photoconversion protocol was adopted from Callahan et al. (2019). Zebrafish embryos at 4 dpf with genotype *Tg(vGlu-t2a:Gal4; UAS:Kaede)* were anesthetized with 0.02% Tricaine and mounted in 1.5% low melting-point agarose. One or two Kaede-expressing neurons at the ventral edge of the spinal cord were targeted for conversion. Photoconversion was performed with a 405 nm laser at maximum intensity using the bleach function on a Zeiss LSM-710 confocal microscope equipped with a 40x W Plan-Apochromat objective. Pulses of scanning over the cell body were repeated in 1 s intervals interleaved with imaging the converted and unconverted fluorescence channels until the signal of the photoconverted protein reached a steady state. Larvae were left in fish water overnight to allow photoconverted protein to diffuse along the axon before remounting for imaging the next day. Neuron morphology was segmented using the simple neurite tracer plugin in ImageJ (Longair et al., 2011).

Channelrhodopsin stimulation

Zebrafish embryos at 5-6 dpf with genotype *Tg(vglut2a:loxP-DsRed-loxP-ChR-GFP; nkx2.2b:Cre-mCherry-NLS)* expressing ChR WideReceiver in the V3 neurons were spinalized at the level of the swim bladder and mounted in 1.5% low melting-point agarose. Agarose was removed around the tail and NMDA was added to a final concentration of 50 μM. After 1 min. incubation time, the tail motion was recorded at a frame rate of 200 Hz and the angle was calculated in real time using custom LabView code. The standard deviation over a 10 ms window of the tail angle was used as proxy for the larva's swimming speed. The entire tail was illuminated with 470 nm blue light at 1.3-5.9 mW/mm^2 with a 3 s on 3 s off cycle for 1 min. This intensity was sufficient to saturate the response of the ChR WideReceiver (Umeda et al., 2013). The NMDA concentration was then increased to 75 μM and 100 μM respectively and the experiment repeated. Fish were excluded if none of the applied NMDA concentrations resulted in clear tail oscillations or if there were not at least 5 swim bouts in the light-off condition (9 excluded out of 19 fish).

Free swimming experiments

To create fish lacking V3 neurons, either *Tg(sim1a:loxP-DsRed-loxP-DTA)*$^{+/-}$ fish were crossed to *Tg(hox4a/9a:Cre)*$^{+/-}$ fish or *Tg(sim1a:loxP-DsRed-loxP-DTA*$^{+/-}$*; hox4a/9aCre*$^{+/-}$*)* fish were out-crossed to wildtype adults. The resulting offspring contained a mix of larvae containing the sim1a:loxP-DsRed-loxP-DTA transgene with or without the Cre recombinase. Larvae were pre-screened for the presence of the *Tg(sim1a:loxP-DsRed-loxP-DTA)* transgene by strong DsRed expression in the brain under low magnification. Experiments were performed blind to Cre expression and hence whether the fish contained V3 neurons. After the experiment, spinal cord expression of DsRed was verified under high magnification to assign 'KO' (larvae lacking V3 neurons) or 'WT' (larvae expressing DsRed in V3 neurons) genotypes.

To verify the ablations of V3 neurons, we crossed *Tg(sim1a:loxP-DsRed-loxP-DTA*$^{+/-}$*; hox4a/9aCre*$^{+/-}$*)* to *Tg(vGlut2a:GFP)* (Satou et al., 2012) and acquired confocal images (Olympus FV1000) to verify the absence of V3 neurons in the ventral spinal cord (Figure 6A)

Larvae at 5-6 dpf were placed in a 76.2 x 15.7 mm arena cast from 3% agarose. The arena was placed on top of diffusive paper (Rosco Cinegel 3000) and illuminated from below with an array of IR LEDs. A video projector (Apeman 5000L) was used to project a grating (spatial period 7.7 mm, rgb values: 0 0 0 or 0 1 1) onto the diffusive paper via a cold mirror. Larva motion was recorded at 300 Hz with an IR-sensitive monochrome camera (Flir, GS3-U3-41C6NIR-C) equipped with a long-pass filter and a photo objective (Sigma Zoom, 18-200 mm). Each larva received 10 minutes of stationary grating followed by 5 s moving grating and 5 s stationary grating for 10 minutes. The order of grating speeds presented was shuffled for each trial and if a larva reached the end of the arena before the end of the 5 s period, the grating was stopped, and the sequence proceeded into the 5s static period. All stimulus presentation and live tracking of the fish were done with the Stytra software package (Štih et al., 2019).

To exclude false positive swim events due to failed video tracking, we excluded all identified bouts with a standard deviation of the instantaneous cycle frequency > 0.07. Fish where the fraction of excluded bouts exceeded 10% were excluded from the analysis (9 excluded out of 77 fish).

QUANTIFICATION AND STATISTICAL ANALYSIS

All statistical analyses were performed in Matlab. Statistical details of experiments including number and type of replicates and statistical tests used can be found in the figures and figure captions, or in the Results section. For t tests, normality of the data was tested by the Kolmogorov-Smirnov test or the Shapiro-Wilk test. The generalized linear models used in Figures 5 and 6 (Tables S1 and S2) did not assume normality of the underlying data.

ChR activation experiments

We sought to test whether blue light optogenetic stimulation (LED) affected bout duration, swim strength or tail beat frequency. Each fish was tested multiple times with and without illumination, and we sought to control for inter-animal differences. We fitted a linear mixed model using the matlab function fitlme, and p-values were obtained using anova on the resulting model. After correcting for multiple hypothesis testing, a significant effect of LED illumination was set at $p \leq 0.0167$. The model and fit are given in Table S1.

Free swimming experiments

In the free swimming experiments, we sought to test whether the genotype had a significant effect on swim speed, bout duration or tail beat frequency as a response to swimming at different OMR grating speeds. We fitted a linear mixed model using the matlab function fitlme, and p-values were obtained using anova on the resulting model. After correcting for multiple hypothesis testing, significance for either genotype or the genotype:omr interaction was set at $p \leq 0.0167$. The model and fit are given in Table S2.

Supplemental information

Voltage imaging identifies spinal circuits

that modulate locomotor adaptation in zebrafish

Urs L. Böhm, Yukiko Kimura, Takashi Kawashima, Misha B. Ahrens, Shin-ichi Higashijima, Florian Engert, and Adam E. Cohen
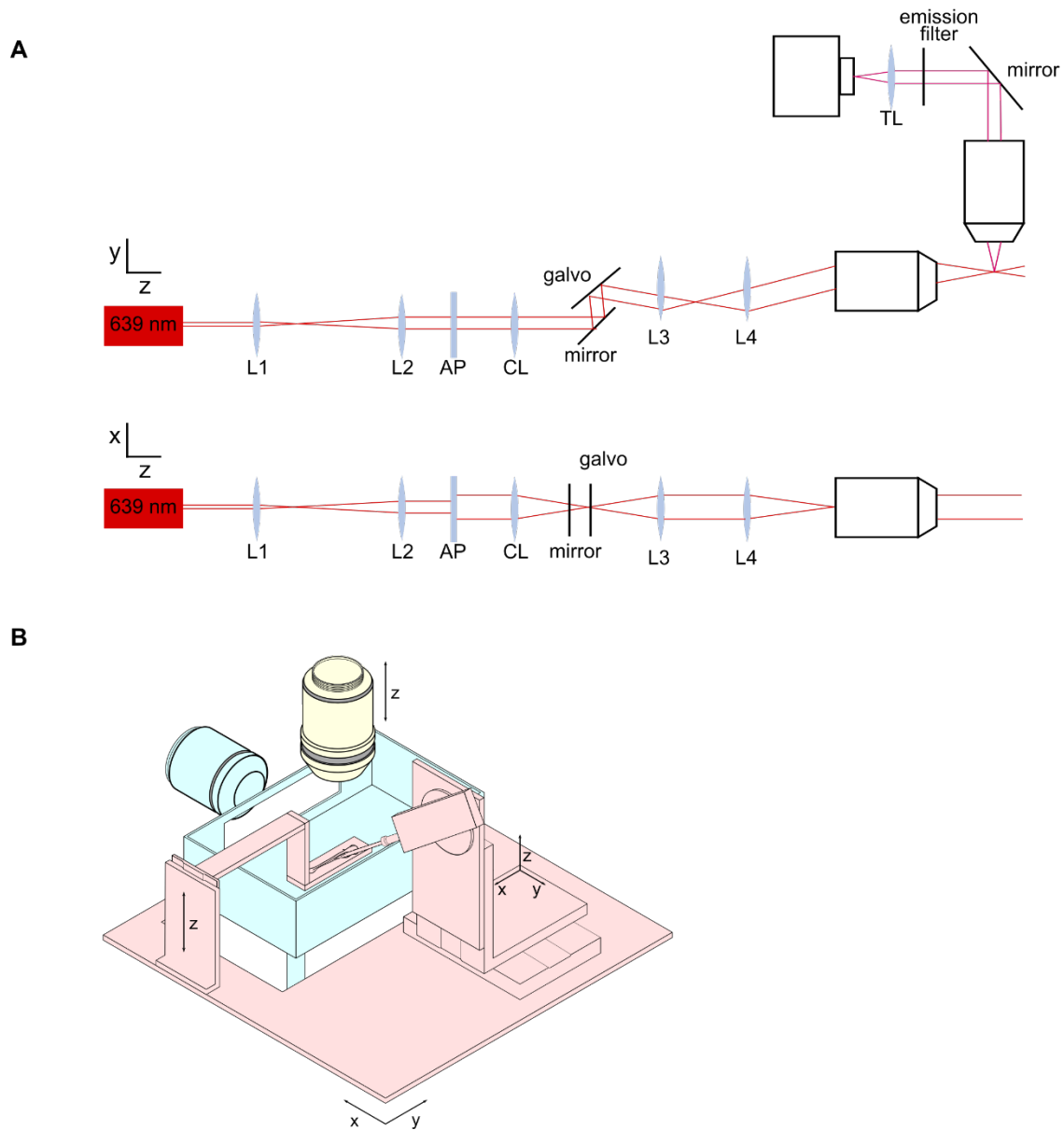
Supplementary figure 1. Light-sheet voltage imaging setup, related to Fig. 1.
(A) Schematic of the optical setup. Side and top view of the excitation beam path showing the beam expander (L1 and L2), anamorphic prism pair to expand the beam along the x-axis, cylindrical lens (Cl), folding mirror and galvo mirror to position the light sheet along the y-axis, scan lens (L3), tube lens (L4) and illumination objective. The emission path contains the imaging objective, folding mirror, emission filter, tube lens (TL) and camera. See Materials and Methods for specifications about the individual components. (B) Sample holder and imaging chamber. Similarly colored elements can move together. Red: sample holder and electrophysiology headstage on x-y stage. Yellow: imaging objective. Blue: sample chamber and illumination objective (fixed).
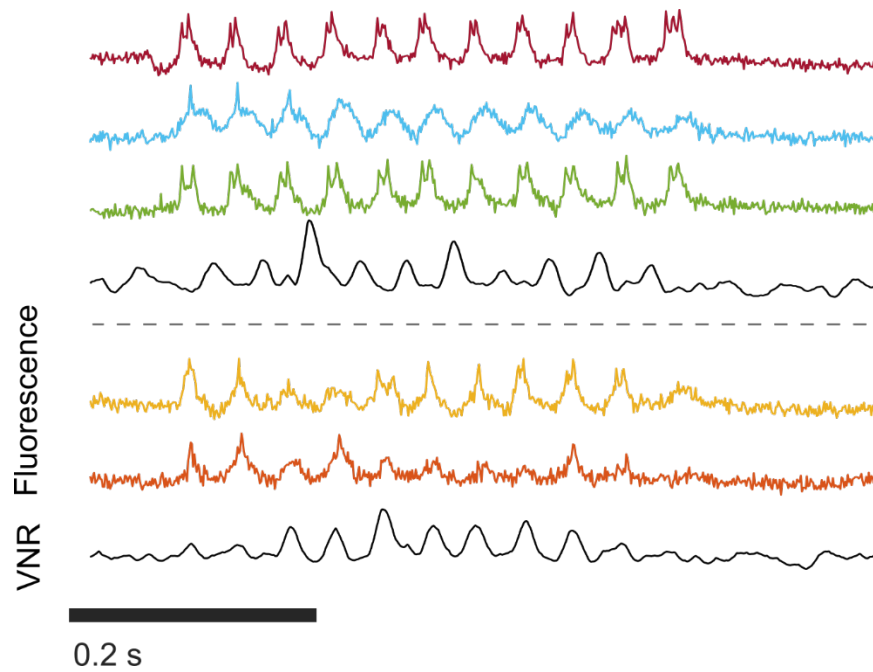
Supplementary figure 2. High SNR recordings show spiking in oscillating neurons, related to Fig. 1.
High SNR optical voltage recordings and corresponding VNR signals from oscillating neurons during a swim bout. Small spikes were visible on top of the larger subthreshold depolarizations. Dashed line separates recordings from different animals.
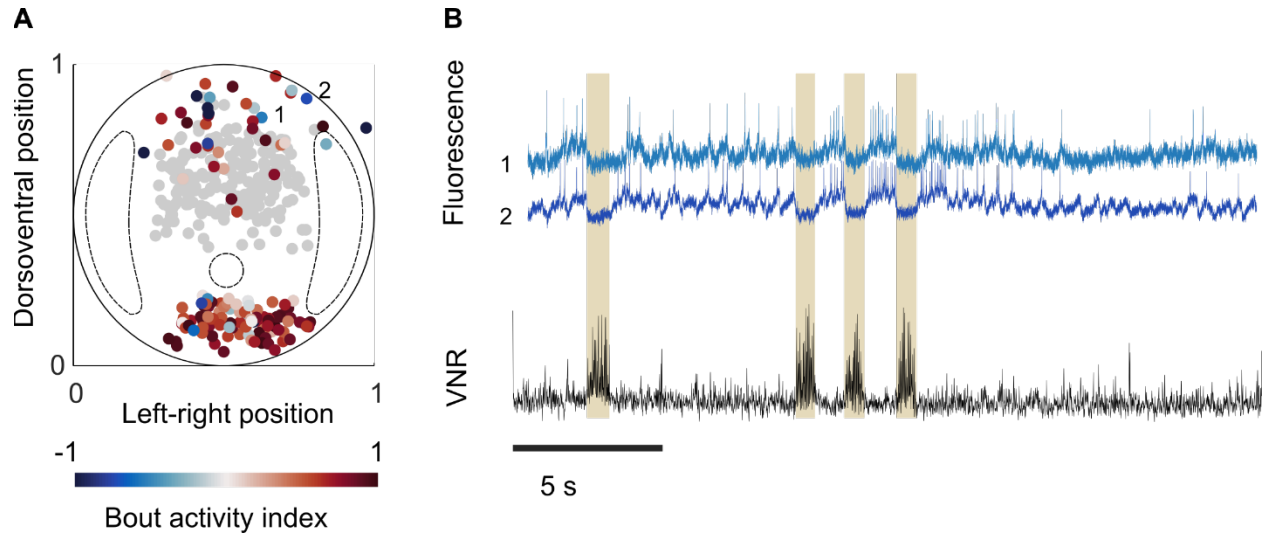
Supplementary figure 3. Distribution of non-oscillating neurons active during bouts and interbout intervals, related to Fig. 1.
(A) Transverse view showing cell body positions of non-oscillating neurons color coded by bout activity index. Oscillating neurons are in gray. Fluorescence traces of numbered neurons are plotted in (B). (B) Fluorescence traces of two dorsal neurons imaged simultaneously showing distinct spiking during interbout intervals and inhibition during swim bouts.

A *vGlut2a:GFP; sim1a:DsRed*

C
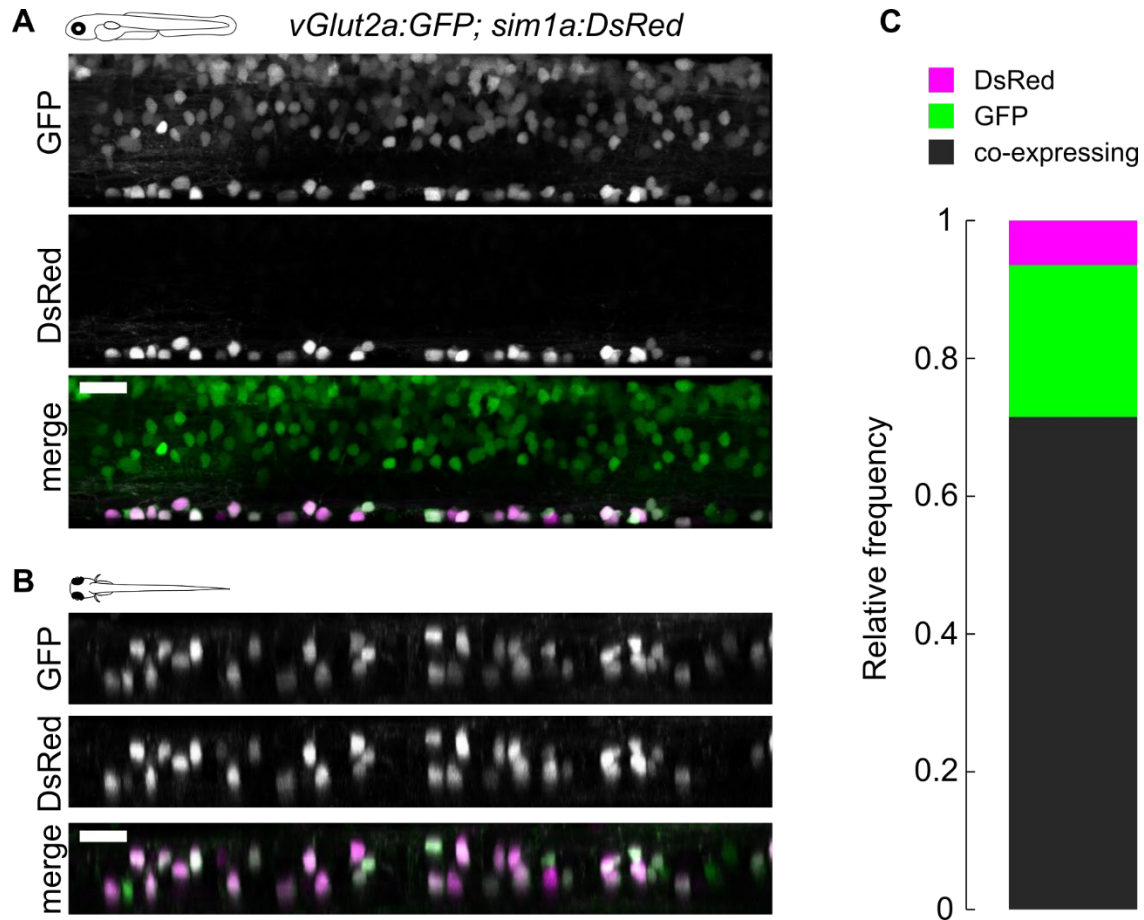
Supplementary figure 4. Quantification of sim1a positive glutamatergic neurons in the ventral spinal cord, related to Fig. 2.

(A) Z-projection of the lateral view of the spinal cord expressing GFP under the control of the *vGlut2a* promotor and DsRed under the control of the *sim1a* promotor. The ventral population of glutamatergic cells is clearly separated from the more dorsal population and most neurons co-express the V3 marker sim1a. (B) Z-projection of the dorsal view of the ventral neurons only. Same field of view as in A. (C) quantification of co-expression of GFP and DsRed from 186 neurons (133 co-expressing, 41 GFP+ only, 12 DsRed+ only) in 3 larvae. Scale bar 20 μm.
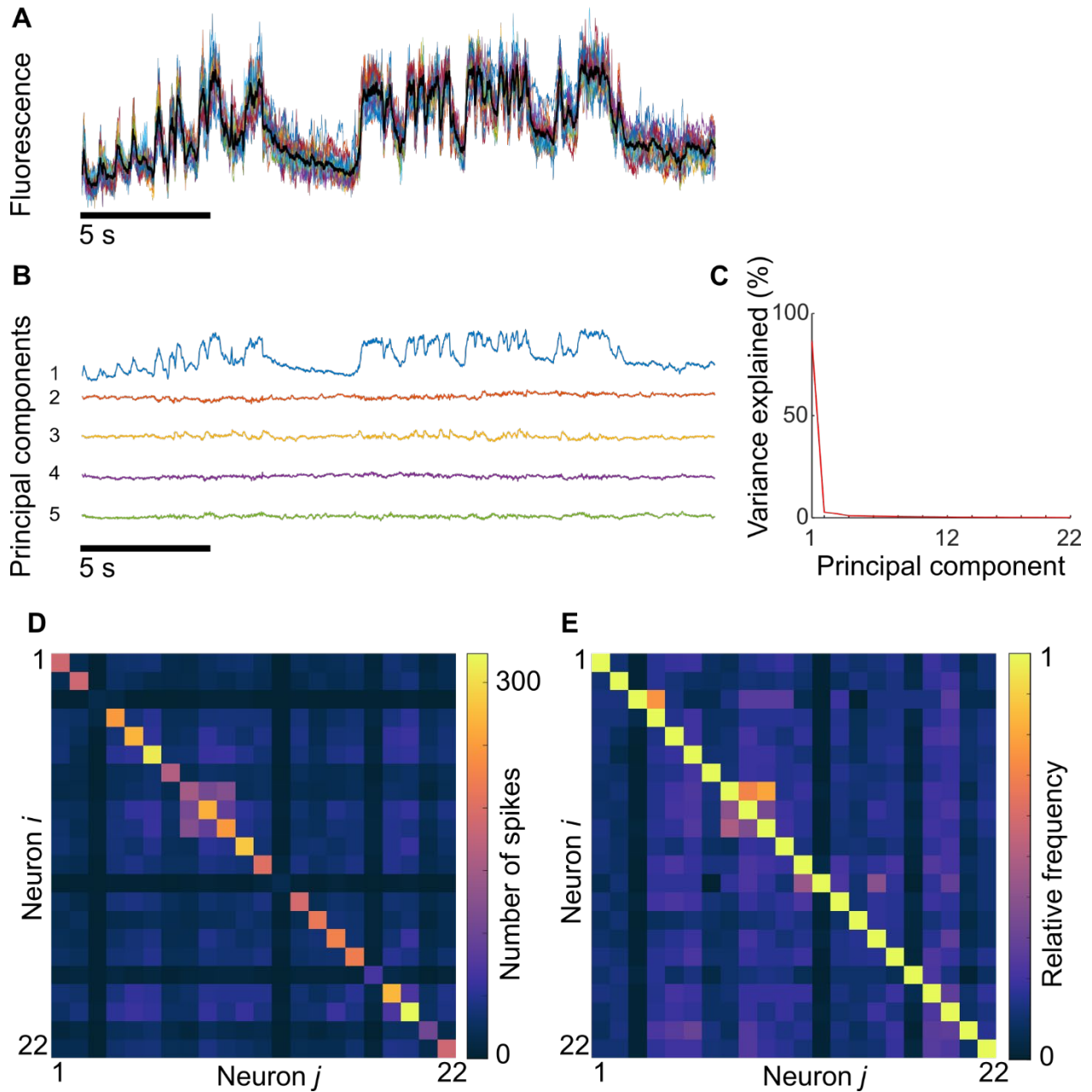
Supplementary figure 5. Subthreshold variation and relative spike timing of V3 neurons, related to Fig. 2 and Fig. 3.
(A) Individual and average subthreshold voltage (spikes removed) of 22 simultaneously recorded V3 neurons. Subthreshold fluctuations were highly synchronized between all neurons. (B) The first five principal components show that most of the subthreshold variance is captured in the first principal component. (C) Percent of variance explained by each of the 22 principal components of the subthreshold voltages. (D,E) Simultaneously occurring spikes of all neurons in the same recording as in (A-B). (D) Total number of spikes in neuron *i* in a 5 ms window around each spike of neuron *j*. (E) Same data as in A, but normalized to the number of spikes in neuron *i*.
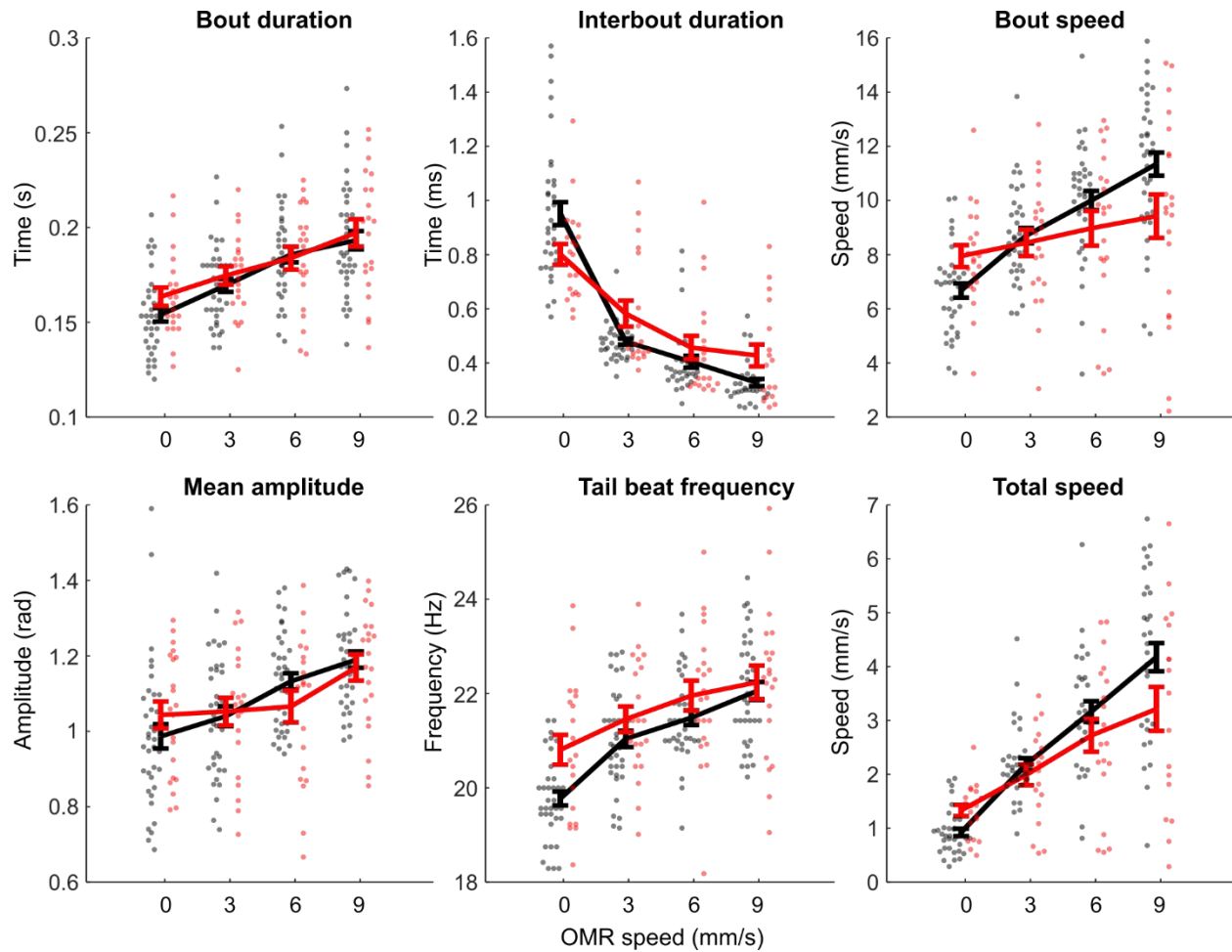
Supplementary figure 6. Kinematics of free-swimming V3 ablated and control larvae, related to Fig. 6

Red: V3 ablated. Black: clutch-matched controls. All parameters were measured as a function of OMR grating speed. Each dot represents the median value for one fish, the line the average value across fish, error bars are s.e.m.

Model: $\log_{10}$(Duration) ~ 1 + LED + (1 + LED | fishID)

	Estimate (log10(ms))	SE	FStat	pValue
(Intercept)	2.7116	0.12176	495.97	1.1074e-84
LED	0.22015	0.08658	6.4657	0.011198

Model: SwimStrength ~ 1 + LED + (1 + LED | fishID)

	Estimate (a.u.)	SE	FStat	pValue
(Intercept)	0.05041	0.0087851	32.926	1.445e-08
LED	0.012388	0.0040424	9.3918	0.0022663

Model: Frequency ~ 1 + LED + (1 + LED | fishID)

	Estimate (Hz)	SE	FStat	pValue
(Intercept)	12.836	0.64597	394.85	1.4986e-69
LED	0.55402	0.26971	4.2196	0.040344

Supplementary Table 1: Fit of linear mixed model to ChR activation data, related to Fig. 5.

Model: speed ~ 1 + omr*genotype + (1 + omr|fishId)

	Estimate (mm/s)	SE	FStat	pValue
(Intercept)	6.8846	0.25526	727.47	2.7028e-72
omr	0.51001	0.052955	92.757	1.3644e-18
genotype	0.901	0.43914	4.2096	0.041358
omr:genotype	-0.34485	0.087244	15.624	0.00010362

Model: duration ~ 1 + omr*genotype + (1 + omr|fishId)

	Estimate (s)	SE	FStat	pValue
(Intercept)	0.1555	0.0033605	2141.2	1.2667e-116
omr	0.0044722	0.00042461	110.93	2.4818e-21
genotype	0.004082	0.0056441	0.52306	0.47029
omr:genotype	-0.00079233	0.00069955	1.2828	0.25858

Model: frequency ~ 1 + omr*genotype + (1 + omr|fishId)

	Estimate (Hz)	SE	FStat	pValue
(Intercept)	19.996	0.17552	12979	2.7737e-200
omr	0.24289	0.015327	251.14	1.9345e-38
genotype	0.74014	0.29456	6.3135	0.012687
omr:genotype	-0.083002	0.025251	10.805	0.0011751

Supplementary Table 2: Fit of linear mixed model to free swimming data, related to Fig. 6.